nature biomedical engineering

Article

https://doi.org/10.1038/s41551-025-01425-5

# Engineering multi-specific nano-antibodies for cancer immunotherapy

Received: 14 October 2023

Accepted: 9 May 2025

Published online: 26 June 2025

Check for updates

Ya-Nan Fan[1], Long Zhu[1], Yu-Xin Qing[1], Si-Yi Ye[1], Qian-Ni Ye[1], Xiao-Yi Huang[1], Dong-Kun Zhao[1], Tai-Yu Tian[1], Fang-Chao Li[1], Guan-Rong Yan[1], Xian-Zhu Yang[1,2], Song Shen[1,2] ✉ & Jun Wang[1,2,3] ✉

Immobilizing multiple types of monoclonal antibody (mAb) on nanoparticle surfaces is a promising approach for creating nanomedicines that emulate the functionality of multi-specific antibodies. However, the clinical translation of these multi-specific nano-antibodies (multi-NanoAbs) has been hindered by intricate fabrication procedures, inevitable attenuation in mAb affinity and insufficient carrier biosecurity. Here we develop a versatile nano-adaptor for immobilizing mAbs and construct multi-NanoAbs using a recombinant fusion protein that consists of Fc gamma receptor 1 and serum albumin, along with the biomedical polymer poly(L-lactide). Our findings demonstrate that fusion protein/polymer-based nano-adaptor is facilitated by FcγR1 on its surface to bind mAbs through receptor–ligand interactions rather than complex chemical conjugation and enables convenient and controlled construction of diverse multi-NanoAbs with efficacious therapeutic effects. We achieved large-scale production of humanized fusion protein/polymer-based nano-adaptor and confirmed the antitumour effectiveness of multi-NanoAb in humanized immune system mouse models, highlighting their prospects for clinical translation.

Multi-specific antibodies, which possess the ability to target more than two epitopes simultaneously, are increasingly acknowledged as pivotal components of next-generation antibody-based therapeutics[1,2]. In contrast to combining separate monoclonal antibodies (mAbs) with distinct mechanisms of action and bispecific antibodies, multi-specific antibodies possess several unique attributes, such as multivalence characteristics, synchronized spatiotemporal regulation of multiple signalling pathways, and possess the capability to simultaneously target two or more immunomodulatory targets while engaging tumour cells, thereby augmenting their antitumour efficacy[3]. However, unlike mAbs that have well-established production processes spanning decades, the functional diversity of multi-specific antibodies presents challenges in terms of manufacturability, which can result in unintended by-products, rendering the manufacturing processes time-consuming, expensive and low yield[4]. In addition, several post-production issues must be addressed, including degradation, aggregation, denaturation and fragmentation, before patients can fully benefit from this strategy[5–7].

Immobilizing multiple types of mAb on the surface of nanoparticles is an alternative and promising strategy for constructing multi-specific nano-antibodies (multi-NanoAbs). Although reported nano-antibodies show antitumour effects, their construction methods involve complicated preparation processes, impairment of mAb function and inadequate carrier biosafety, which ultimately restrict their clinical translation[8–10]. For example, cumbersome chemical coupling and non-directional immobilization strategies may weaken the activity of antibodies or hinder the antigen recognition sites. Anti-Fc antibody-coated aminated polystyrene nanoparticles could serve as

[1]School of Biomedical Sciences and Engineering, South China University of Technology, Guangzhou International Campus, Guangzhou, P. R. China. [2]National Engineering Research Center for Tissue Restoration and Reconstruction, South China University of Technology, Guangzhou, P. R. China. [3]Guangdong Provincial Key Laboratory of Biomedical Engineering, South China University of Technology, Guangzhou, P. R. China. ✉e-mail: shensong@scut.edu.cn; mcjwang@scut.edu.cn

an antibody immobilization platform[11,12]. However, the poor biocompatibility of polystyrene nanocarriers, complicated anti-Fc antibody conjugation procedures and unsuitability for large-scale production prevent them from being ideal antibody anchors[13,14].

Given the remarkable affinity of Fc gamma receptor 1 (FcγR1), a type of Fc receptor extensively expressed on immune cells such as macrophages, for Fc fragments of immunoglobulin G (IgG)[15–18], we propose that FcγR1-coated nanoparticles could effectively immobilize mAbs with conserved Fc fragment. Furthermore, considering the presence of hydrophobic binding domains for long-chain fatty acids (LCFAs) within serum albumin (SA) (the most abundant circulating plasma protein)[19,20], we put forth innovative concepts wherein albumin can assemble with hydrophobic aliphatic polyesters (for example, polylactic acid) to form stable nanoassemblies using an ultrasonic method or high-pressure homogenization. By merging the aforementioned concepts, herein we have constructed a versatile platform for mAb immobilization and multi-NanoAb construction using genetically engineered fusion protein comprising FcγR1 and SA along with poly(L-lactide) (PLLA), which we have named fusion protein/polymer-based nano-adaptor (FP-NA). Compared with previous works, FP-NA exhibits several improvements and advantages. First, its composition is simplified as it only requires fusion protein FcγR1–SA and PLLA without needing an anti-Fc antibody. Second, it bypasses intricate chemical reactions and reagent application requirements. Third, it is suitable for large-scale production through a streamlined one-step process. Our findings demonstrate that FP-NA, facilitated by the presence of FcγR1 on its surface, enables convenient and controlled construction of various multi-NanoAbs, whose efficient therapeutic effects were validated in several mouse tumour models (Fig. 1a,b). We successfully developed humanized FP-NA, scaled up their production processes and confirmed the antitumour effect of multi-NanoAbs in humanized immune system mouse models. It is believed that multi-NanoAbs constructed from FP-NA and mAbs hold immense potential for treating diseases beyond tumours.

## Results

### Design and characterization of FP-NA

As an abundant plasma protein, SA possesses hydrophobic pockets with remarkable affinities for LCFAs, metabolites and other molecules[21,22]. The renowned nanomedicine, albumin-bound active ingredient(active ingr. ), created by attaching active ingredient to these hydrophobic pockets using igh-pressure homogenization techniques[23–25]. Drawing inspiration om this approach, the fusion protein (FcγR1–SA) was designed by nking the extracellular fragment of mouse FcγR1 (mFcγR1) and mouse erum albumin (MSA) via a $(G_4S)_2$ linker, with a His tag incorporated t the carboxy terminus for purification (Fig. 2a). We postulated that ydrophobic polyesters such as PLLA can form stable nanoparticles hrough their interaction with mFcγR1–MSA fusion proteins. Molecular dynamics simulations demonstrated that PLLA (molecular weight ($M_w$) = 36 kDa) is intricately wrapped around and partially embedded within mFcγR1–MSA fusion proteins to form a complex. Calculations indicated a theoretical binding free energy between PLLA and mFcγR1–MSA at about −1,833 kJ $mol^{-1}$, signifying their stable combination through multiple interactions (Fig. 2b and Supplementary Fig. 1). The primary contributors to this stability included negative energy terms such as electrostatic interaction energy, van der Waals energy and nonpolar solvation energy, while positive polar solvation energy had a minimal impact on it (Fig. 2c).

The *mFcγR1–MSA* gene expression vector was successfully constructed in recombinant *Pichia pastoris*, and the fusion protein product was initially evaluated by using sodium dodecyl sulfate–polyacrylamide gel electrophoresis (Supplementary Fig. 2). The purified mFcγR1–MSA was characterized by fast protein liquid chromatography (Supplementary Fig. 3) and ultra-performance liquid chromatography (Supplementary Fig. 4). Subsequently, the peptide mapping was conducted using liquid chromatography-tandem mass spectrometry (LC-MS/MS) (Supplementary Fig. 5), while western blotting analysis confirmed the presence of functional components, including mFcγR1, MSA and His tag (Fig. 2d). Enzyme-linked immunosorbent assay (ELISA) confirmed that mFcγR1–MSA exhibited an almost indistinguishable affinity curve for IgG2a mAbs compared with the commercial recombinant mFcγR1, with comparable $K_d$ values (Fig. 2e). Interestingly, the affinity curves of mFcγR1–MSA for various IgG2a mAb subtypes demonstrate equivalent upper and lower plateau phases, while their affinity constants ($K_d$ values) remain consistently within a narrow range of 12–20 nM (Fig. 2f), indicating that the mFcγR1–MSA-derived nano-adaptor holds the potential to serve as a universal immobilization platform of mAbs with conserved Fc segment.

The construction of FP-NA was accomplished through a single ultrasonic emulsification and solvent evaporation technique. After determining the optimal water–oil ratio (5:1) and protein–polymer mass ratio (5:1) during preparation, we further fine-tuned the $M_w$ of PLLA within a range spanning from 1.5 kDa to 1,100 kDa to achieve an exquisite optimization of FP-NA construction (Fig. 2g). Marked precipitation was observed during the preparation process when the $M_w$ of PLLA reached or exceeded 240 kDa (Supplementary Fig. 6), while the $M_w$ less than 7.2 kDa resulted in the generation of FP-NA with poor dispersibility, indicating that excessively small or large $M_w$ of PLLA do not facilitate their assembly with mFcγR1–MSA. When the $M_w$ of PLLA falls within the range of 7.2–159 kDa, the size range of FP-NA assembled by mFcγR1–MSA and PLLA is 115–125 nm, with a polydispersity index (PDI) of 0.13–0.18 (Fig. 2h). The monitoring of FP-NA quantity reveals that when the $M_w$ of PLLA is at 130 kDa, it yields the highest number of particles under identical conditions with relatively minimal variation (Supplementary Fig. 7). Moreover, the stability of initially selected FP-NAs in 1× PBS and DMEM medium supplemented with 10% fetal bovine serum (FBS) was evaluated using dynamic light scattering (DLS) and scanning electron microscopy (SEM), revealing that FP-NAs composed of mFcγR1–MSA and PLLA130K exhibit uniform particle sizes, regular spherical structures and exceptional stability (Fig. 2i,j and Supplementary Figs. 8 and 9). To explore the assembly mechanism, dissipative particle dynamics simulation was used to elucidate the dissipative self-assembly process of mFcγR1–MSA and PLLA with different $M_w$. As depicted in Supplementary Fig. 10, it is evident that an inadequate or excessive $M_w$ does not promote the formation of well-defined is nanoscale particles. In cases where the $M_w$ of PLLA is suboptimal, the h assembled particles exhibit heterogeneity and a loose structure, making fr them susceptible to rapid disintegration upon interaction with proteins li owing to their inherent structural instability. We also confirmed s that the combination of chloroform-dissolved PLLA130K with water a (without mFcγR1–MSA), the mixture of mFcγR1–MSA with chloroform h (without PLLA), or directly mixing of mAbs with the PLLA130K, followed t by sonication and solvent evaporation did not result in successful assembly into nanoscale particles (Supplementary Fig. 11). On the basis of the aforementioned results, we have discovered that only PLLA with an appropriate $M_w$ facilitates easier assembly of mFcγR1–MSA into nanoparticles with uniform size and exceptional stability, leading us to propose several potential explanations: (1) albumin possesses seven binding sites for LCFAs, and PLLA, an aliphatic polyester material, has the potential to bind to these albumin binding sites of mFcγR1–MSA; (2) excessively large $M_w$ of PLLA leads to strong intermolecular forces causing steric hindrance, while excessively low $M_w$ results in strong end-effect interactions with the solvent, which is unfavourable for assembly; and (3) when assembled into FP-NA, the intricate intertwining among PLLA molecules themselves and with mFcγR1–MSA, as well as combined effects of electrostatic energy, van der Waals energy and nonpolar solvation energy between mFcγR1–MSA and PLLA further ensure the stability of FP-NA after construction.

The successful assembly of mFcγR1–MSA (labelled with Alexa Fluor 488) and PLLA130K (labelled with rhodamine B) was

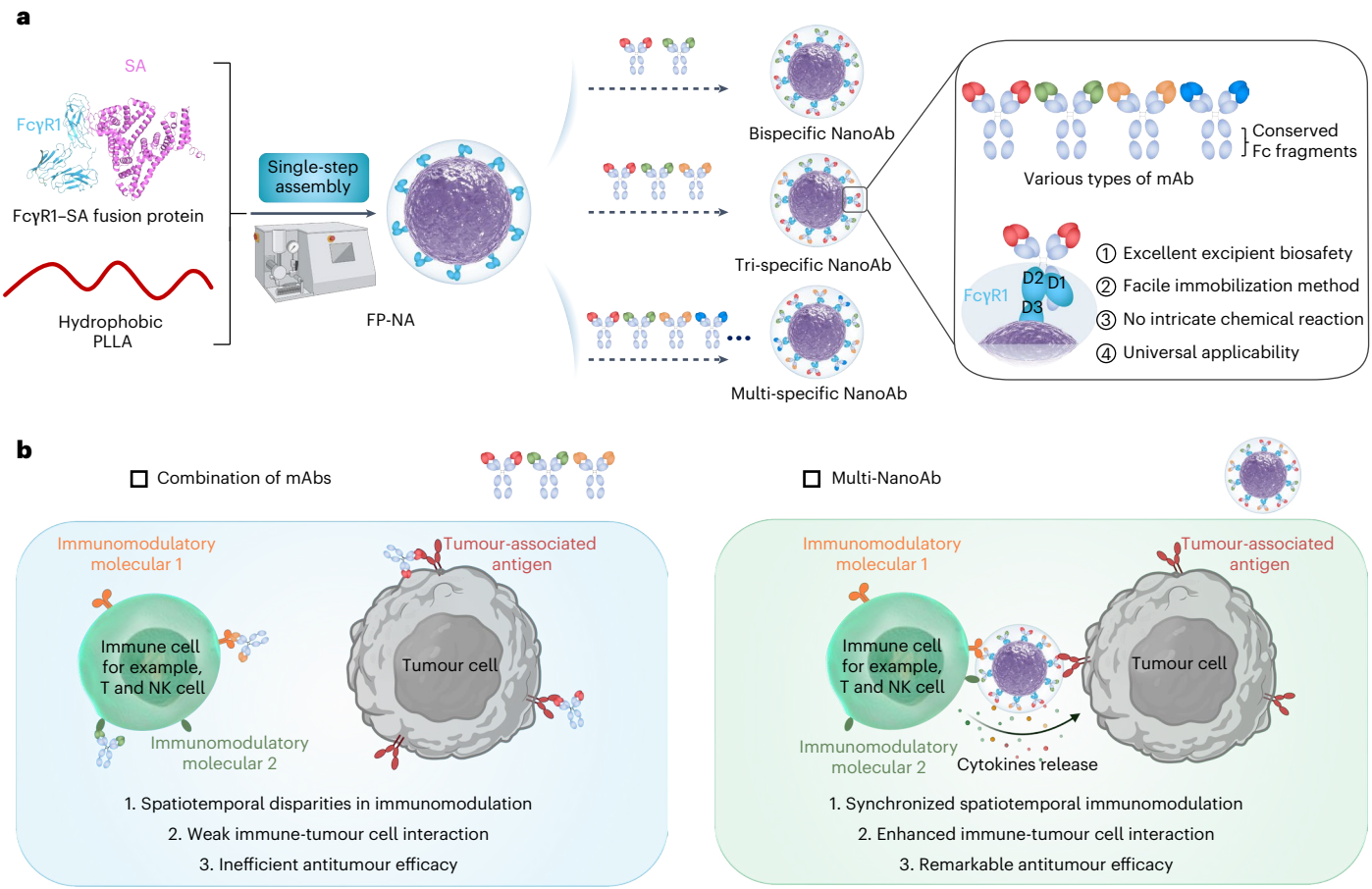


**Fig. 1 | Schematic illustrating the design of FP-NA and multi-NanoAb with the potential to improve mAb-based cancer immunotherapy. a**, The fusion protein FcγR1–SA and hydrophobic PLLA, two excipients with exceptional biosafety, can be assembled into a biocompatible FP-NA through a simplified one-step method. The optimized FP-NA exhibited an average molecular weight of $2.412 \times 10^8$ Da, with the mass and quantity ratios of FcγR1–SA to PLLA being 49.85:50.15 and 1,252:930, respectively. FP-NA exhibits remarkable versatility in immobilizing mAbs and facilitating the binding of multiple mAbs by leveraging the interaction between FcγR1 (receptor) and Fc (ligand), thereby eliminating the need for intricate chemical reactions and enabling convenient and controlled construction of diverse multi-NanoAbs. **b**, Compared with combining individual mAbs with distinct mechanisms of action, multi-NanoAbs possess unique attributes, such as synchronized spatiotemporal regulation of multiple signals and enhanced immune-tumour cell interaction, resulting in more remarkable antitumour efficacy. This figure was created with BioRender.com under a CC-BY-NC-ND licence.

subsequently confirmed by their co-localization examined by stochastic optical reconstruction microscopy (STORM) imaging (Fig. 2k) and NanoFCM analysis (Fig. 2l). An analysis of the mFcγR1–MSA content in FP-NA was conducted using a Kjeldahl nitrogen analyser, followed by freeze-drying and weighing of the total mass of FP-NA, ultimately revealing that mFcγR1–MSA accounted for a 49.85% of FP-NA's composition. By means of size exclusion chromatography with multi-angle static light scattering, an average molecular weight of $2.412 \times 10^8$ Da for FP-NA was obtained (Supplementary Fig. 12), enabling us to calculate a number ratio of 1,252:930 between mFcγR1–MSA and PLLA130K in each FP-NA.

The mAb-binding capability of mFcγR1–MSA exposed to chloroform and sonication remained comparable to that of the original counterpart, indicating that the construction process of FP-NA had a negligible impact on its affinity (Supplementary Fig. 13). Thus, the functionality of mFcγR1–MSA presented on FP-NA would also remain unaltered. The definitive confirmation of FP-NA's binding capability to the Fc segment of the antibody, aided by the mFcγR1 domain, was established through precise monitoring of thermal variations during their interactions utilizing isothermal titration calorimetry (ITC). Following the addition of IgG2a mAbs to FP-NA, an impactful exothermic response was observed, whereas minimal heat alteration was detected in the $NP_{MSA/PLLA}$ control group. This clearly signified a distinctive and selective interaction between FP-NA and IgG2a mAbs (Fig. 2m). FP-NA exhibited a heightened affinity towards mAbs when compared with free mFcγR1–MSA (Supplementary Fig. 14). We postulated that while a fraction of the mFcγR1 might be located within the core of FP-NA, the majority was shown on its surface, presenting as a 'multivalent state' characterized by multiple instances of mFcγR1 on a single particle. Consequently, this configuration exhibits an enhanced affinity for mAbs. The energy spectrum analysis of FP-NA binding with colloidal gold-labelled antibodies proved that the mAbs were bound to the surface of FP-NA (Supplementary Fig. 15). Following the labelling of mFcγR1–MSA with Alexa Fluor 488 and its assembly onto FP-NA, incubation with Alexa Fluor 555-labelled mAbs resulted in multiple binding events between mAb molecules and the particle surface, as directly confirmed by NanoFCM analysis and STORM observation. This compelling evidence unequivocally supports the presence of mFcγR1 on the surface of FP-NA (Supplementary Fig. 16). The mAb-binding capability of FP-NA was further quantitatively ascertained using ELISA. As illustrated in Fig. 2n, when the mass ratio of mFcγR1–MSA in FP-NA to mAbs reached 10:1, an impressive immobilization efficiency of approximately 95% was achieved, establishing this ratio as the optimal choice for subsequent experiments. Moreover, under these circumstances, the average quantity (valence) of antibodies immobilized on each FP-NA was calculated to be around 117 (Supplementary Fig. 17).

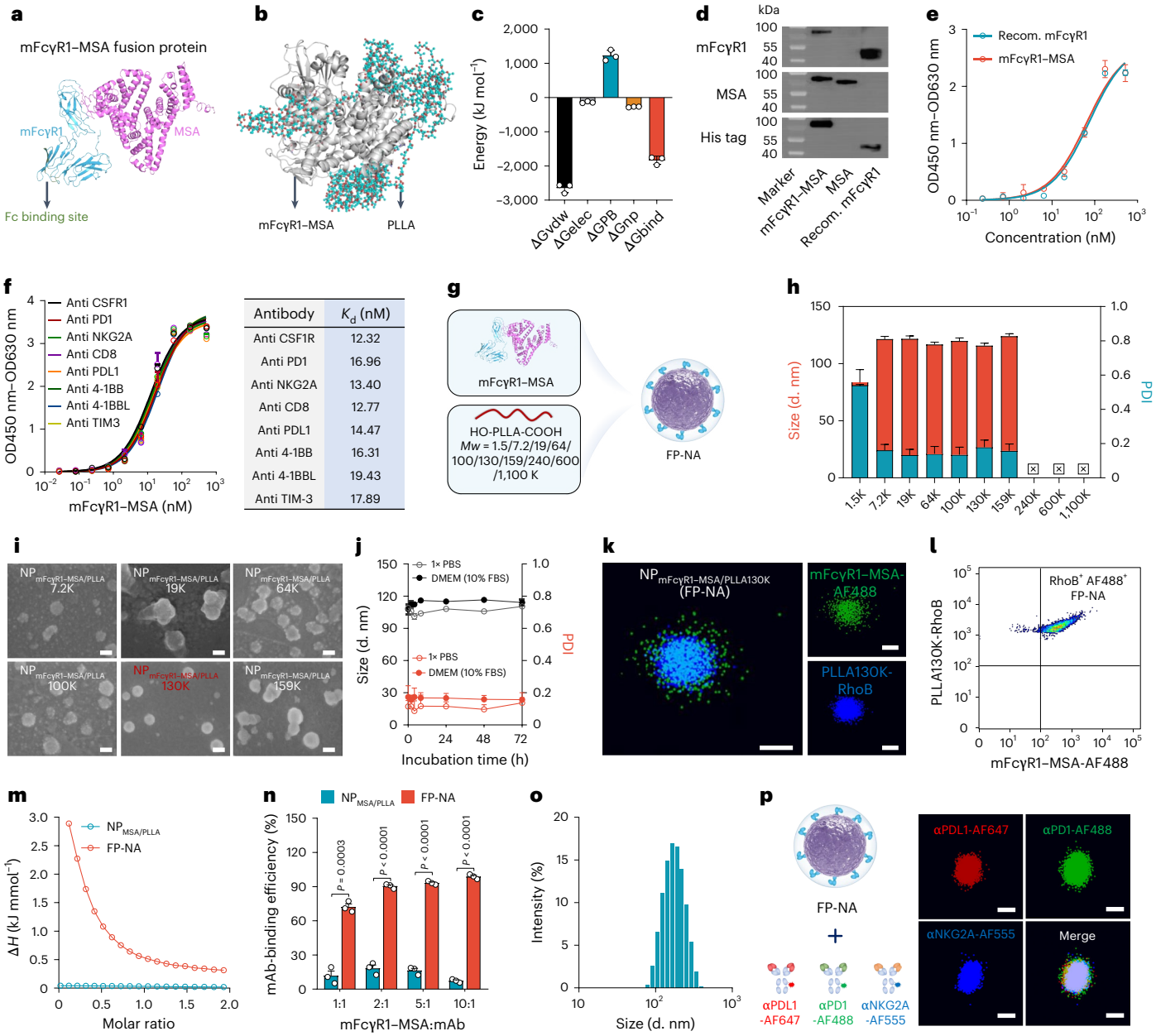


**Fig. 2 | The construction and characterization of FP-NA. a**, 3D structure prediction for mFcγR1–MSA fusion protein. **b**, Molecular dynamics simulation of complexation between mFcγR1–MSA and PLLA. **c**, The free energy of binding and individual energy terms in the system. Data are presented as mean ± s.d. ($n = 3$ independent calculation). **d**, Western blot analyses of the main components (mFcγR1, MSA and His tag) of mFcγR1–MSA. **e**, The binding curve of IgG2a to mFcγR1–MSA (red) and recombinant mFcγR1 (blue) by single-antigen captured ELISA at the indicated concentration. Recom. mFcγR1, recombinant mFcγR1. Data are presented as mean ± s.d. ($n = 3$ biologically independent samples). **f**, The binding curve and $K_d$ value of multiple mAbs to mFcγR1–MSA. Data are presented as mean ± s.d. ($n = 3$ biologically independent samples). **g**, Scheme of the $M_w$ of PLLA for screening the optimal formula for FP-NA. **h**, Average hydrodynamic size and PDI of FP-NAs prepared using different $M_w$ of PLLA as determined by DLS. Data are presented as mean ± s.d. ($n = 5$ biologically independent samples). **i**, Representative SEM images of FP-NAs prepared by PLLA7.2K–159K. Scale bars, 100 nm. FP-NAs were incubated in 1× PBS for 7 days before imaging. **j**, Average hydrodynamic size and PDI variation of FP-NA prepared using PLLA130K in 1× PBS and DMEM (containing 10% FBS) during incubation for 72 h. Data are presented as mean ± s.d. ($n = 5$ biologically independent samples). **k**, Representative STORM images of FP-NA. mFcγR1–MSA and PLLA were labelled with AF488 (green) and RhoB (blue), respectively. Scale bars, 60 nm. **l**, The bivariate dot plots of the FP-NA (mFcγR1–MSA labelled with AF488, and PLLA labelled with RhoB) were detected using NanoFCM. **m**, The analysis of the binding of IgG2a to FP-NA (red) and $NP_{MSA/PLLA}$ (blue) by ITC. The experiment was replicated three times, yielding similar results. **n**, The mAb-binding efficiency of FP-NA (red) and $NP_{MSA/PLLA}$ (blue). Data are presented as mean ± s.d. ($n = 3$ biologically independent samples). **o**, The size distribution of Tri-NanoAb was detected by DLS. d.nm, diameter (nm). The experiment was replicated three times, yielding similar results. **p**, Representative STORM images of FP-NA binding with three types of antibody; αPDL1, αPD1 and αNKG2A were labelled with AF647 (red), AF488 (green) and AF555 (blue), respectively. Scale bars, 60 nm. The $P$ values in **n** were generated using two-tailed Student's $t$-test. $^{***}P < 0.001$, $^{****}P < 0.0001$. For **d**, **i**, **k**, **l** and **p**, experiments were repeated three times, yielding similar results, and a representative image was provided.

Furthermore, a tri-specific nano-antibody (Tri-NanoAb) targeting PDL1/PD1/NKG2A was engineered to assess the potential of FP-NA in different types of mAb. The Tri-NanoAb had homogeneous particle size distribution (Fig. 2o) with weakly negative ζ potential (Supplementary Fig. 18). To quantify the amount of bound mAbs on the FP-NA's surface, αPDL1, αPD1 and αNKG2A were labelled

with Alexa Fluor 647, Alexa Fluor 488 and Alexa Fluor 555, respectively. The high-performance liquid chromatography (HPLC) analysis result confirmed that manipulating the feeding ratio of antibodies enables us to precisely manipulate their proportionate distribution on FP-NA (Supplementary Fig. 19). The STORM images revealed the simultaneous presence of three distinct fluorescent signals (red, green and blue) (Fig. 2p). The exceptional stabilities of FP-NA and NanoAbs were also validated; neither rapid disintegration in FP-NA nor notable swift loss of immobilized antibodies from it is observed (Supplementary Fig. 20). Importantly, Tri-NanoAb exhibits a slightly superior binding affinity towards corresponding target antigens compared with the free mAbs, which can be attributed to the multivalent state of mAbs presented on FP-NA (Supplementary Fig. 21), and the function of each specificity in the Tri-NanoAb does not overshadow or affect others (Supplementary Fig. 22). These results unequivocally demonstrate that FP-NA has an unparalleled capability to immobilize diverse types of mAb with different functions and can serve as a versatile platform for constructing multi-NanoAbs.

### Tri-NanoAb promotes T cell-mediated cytotoxicity in vitro

Generating multi-NanoAbs involves immobilizing multiple types of mAb onto the surface of FP-NA, thereby imparting both multi-specificity (in terms of mAb diversity) and multi-valency (in terms of mAb quantity) to them. We proposed that these distinctive features may endow multi-NanoAbs with unparalleled advantages over the combination of mAbs to facilitate effect–target cell interaction and enhance the antitumour immune response. Here PDL1/PD1/NKG2A Tri-NanoAb was constructed as an illustrative example to investigate the therapeutic advantages of multi-NanoAb. The αPDL1 component of Tri-NanoAb is designed to specifically recognize tumour cells overexpressing PDL1 (programmed death-ligand 1), while αPD1 and αNKG2A were meticulously selected for blocking PD1 (programmed death 1) and NKG2A (NK group 2 member A), respectively, which are two types of inhibitory receptor expressed on T cells with different immunosuppressive mechanisms[26–28]. The combination of fluorescently labelled αPDL1, αPD1 and αNKG2A (referred to as mAbs Comb.) and their corresponding Tri-NanoAb counterparts were incubated with mouse B16F10 melanoma cells and primary $CD8^+$ T cells, followed by confocal laser scanning microscopy observation. As shown in Fig. 3a,b, only AF647-αPDL1 exhibited a remarkable binding affinity towards tumour cells, while exclusively AF488-αPD1 and AF555-αNKG2A demonstrated binding affinities towards T cells within the mAbs Comb. group. Notably, in the Tri-NanoAb group, the surface of tumour cells can be adorned with αPD1 and αNKG2A through the facilitation of αPDL1. Similarly, T cell surfaces can exhibit the emergence of αPDL1 with the assistance of both αPD1 and αNKG2A; this distinctive cell-binding characteristic enables the Tri-NanoAb to serve as a mediator between tumour cells and T cells, effectively promoting their interaction. As depicted in Fig. 3c, the presence of Tri-NanoAb in the co-culture system resulted in remarkable adhesion between T cells and tumour cells, whereas mAbs Comb. lacked this capability. A minimal level of same-type cell adhesion was observed in the high-dose Tri-NanoAb treatment group, which was absent in the mAbs Comb.-treated group. Owing to its multi-valency and multi-specificity properties, it is plausible that Tri-NanoAb induces some degree of same-type cell adhesion, but no fratricidal behaviour among T cells was observed (Supplementary Fig. 23). To further validate the efficacy of Tri-NanoAb in vitro, luciferase-expressing B16F10 cells (B16F10-Luc) were co-cultured with $CD8^+$ T cells in the presence of varying concentrations of mAbs. Compared with mAbs Comb., Tri-NanoAb demonstrated superior effectiveness in augmenting T cell cytotoxicity against tumour cells, particularly at lower concentrations (Fig. 3d). Gene expression profiling has helped understand the biological processes between tumour cells and T cells under the influence of Tri-NanoAb. Figure 3e shows a stacked bar plot of differentially expressed genes between the Control IgG, mAbs Comb. and Tri-NanoAb. Among the differentially expressed genes, the transcripts of 105 genes were upregulated, whereas the transcripts of 113 genes ($|\log_2(\text{fold change})| > 1$) were downregulated in the Tri-NanoAb group compared with those in the mAbs Comb. group (Supplementary Fig. 24). Gene set variation analysis (GSVA) of Gene Ontology (GO) was performed to determine the biological features among the groups using a heat map (Fig. 3f). Altered expression of genes related to T cell function indicated that Tri-NanoAb could enhance the cytotoxicity of T cells against tumour cells. As expected, Tri-NanoAb-treated T cells exhibited the most potent tumour-killing capacity compared with bispecific NanoAbs, Tri-mAbs and the combination of three Mono-NanoAbs (Supplementary Fig. 25). This can be attributed to Tri-NanoAb's superior ability to activate T cells through the synergistic combination of αPD1 and αNKG2A while relying on its remarkable recognition capabilities for both T cells and tumour cells. Consequently, it facilitates heightened cellular interactions and physical proximity, which enables cytotoxic cytokines secreted by T cells to induce apoptosis in neighbouring tumour cells.

### In vivo behaviour of Tri-NanoAb

Before investigating the antitumour potential of PDL1/PD1/NKG2A Tri-NanoAb, its in vivo behaviours, including blood circulation, tumour accumulation and biosafety, were comprehensively evaluated. As shown in Fig. 3g, the blood concentration of fluorescently labelled mAbs exhibited a more gradual decline in mice treated with Tri-NanoAb compared with the mAbs Comb. group; even after 72 h, the antibody content in the blood still accounted for 34% of the initial injection dose. Meanwhile, a majority of mAbs Comb. or Tri-NanoAb were predominantly found within the serum rather than being bound to blood cells (Supplementary Fig. 26). Fluorescently labelled mAbs, either as a free combination or Tri-NanoAb, were then intravenously administered to mice harbouring orthotopic 4T1 breast tumours. At 24 h, 48 h and 72 h post-administration, the major organs (heart, liver, spleen, lung and kidney) and tumour tissues were collected for detection using an IVIS imaging system. As depicted in Fig. 3h,i, both groups observed a considerable accumulation of mAbs in the tumour tissue. It is noteworthy that the fluorescence signal at the tumour site was gradually attenuated after 48 h in the mAbs Comb.-treated mice. Conversely, it continued to increase in the Tri-NanoAb group, with fluorescence intensity approximately 1.5 times higher than that of its free counterpart at the 72 h time point. In addition, a small fluorescence signal was present in other organs (Supplementary Fig. 27). Imaging of live mice and excised major organs from treated mice revealed a slightly higher accumulation of Tri-NanoAb in the liver and lung compared with mAbs Comb. at the 24 h time point. Over time, as metabolic clearance occurred, the fluorescence signal in the livers gradually diminished, reducing the disparity between the mAbs Comb. and Tri-NanoAb groups. Both mAbs Comb. and Tri-NanoAb could recognize and bind to corresponding targets expressed by tumour cells and tumour-infiltrating T cells, thereby facilitating their accumulation within tumour tissues. Owing to its multivalent effect, Tri-NanoAb showed an enhanced affinity towards both tumour cells and T cells while forming tighter associations with them compared with free mAbs; this ultimately facilitated a prolonged retention time within the tumour tissue (Supplementary Fig. 28). Confocal laser scanning microscopy further confirmed that after administration for either 48 h or 72 h, Tri-NanoAb exhibited superior levels of enrichment within tumour sites (Fig. 3j). In addition, as a nanoparticle measuring approximately 120 nm, Tri-NanoAbs possess the fundamental characteristics of conventional nanoparticles while harnessing the enhanced permeability and retention (EPR) effect for accumulation as well as using convection and diffusion mechanisms to achieve deeper tissue penetration. Furthermore, we demonstrated that the binding of Tri-NanoAb on peripheral blood T cells and their infiltration into tumours may contribute to the penetration of Tri-NanoAbs to some extent (Supplementary Figs. 29 and 30).

These findings indicate that Tri-NanoAb can prolong the residence time of mAbs within tumour sites, enabling them to exert their intended functions more efficiently.

Subsequently, the biosafety of the FP-NA and PDL1/PD1/NKG2A Tri-NanoAb was evaluated. Healthy BALB/c mice were administered with mAbs Comb. or Tri-NanoAb (doses of 2.5 mg $kg^{-1}$ of αPDL1, αPD1 and αNKG2A) every 3 days for a total of 3 injections (q3dx3). An FP-NA/Iso group (FP-NA-immobilized IgG2a isotype control antibody) was also included. Blood samples and main organs were collected for examination 3 days after the last injection. As depicted in Fig. 3k–n, compared with the control group, critical indicators of hepatic and renal function, including aspartic acid transaminase (AST), alanine transaminase (ALT), and blood urea nitrogen (UREA), did not exhibit any statistically significant differences among mice treated with FP-NA/Iso, mAbs Comb. and Tri-NanoAb ($P > 0.05$). Similarly, creatine kinase (CK), an index of cardiac function, did not show any elevation in the treatment groups. Furthermore, 1 week and 3 months after completion of the administration period, tissue sections of the main organs (heart, liver, spleen, lung and kidney) were subjected to haematoxylin and eosin (H&E) staining to evaluate whether the drugs caused any pathological changes in these organs. As illustrated in Fig. 3o and Supplementary Fig. 31, the H&E staining results across all groups showed no notable pathological alterations in the tissue structure within each examined organ. These data suggest that at this dosage and frequency of injection, FP-NA/Iso, mAbs Comb. and Tri-NanoAb did not induce notable toxic side effects.

### Tri-NanoAb enhances antitumour immunity in vivo

After confirming the potent augmentation of T cell cytotoxicity against tumour cells in vitro by Tri-NanoAb and its remarkable ability to accumulate efficiently within tumour tissue, we conducted a series of experiments to assess its in vivo antitumour efficacy. The orthotopic 4T1 breast cancer model exhibits molecular similarities with advanced triple-negative breast cancer in humans (stage IV), with a meagre response rate to PD1/PDL1 axis-related blocking therapy. The therapeutic effects of control, FP-NA/Iso, mAbs Comb. and Tri-NanoAb were initially compared in a mouse orthotopic 4T1 breast cancer model (Fig. 4a). As illustrated in Fig. 4b,c, treatment with Tri-NanoAb extensively suppressed the growth rate of 4T1 tumours and led to complete tumour regression in certain mice. By contrast, the administration of mAbs Comb. only delayed tumour progression during the early stages of treatment. The exceptional antitumour effect of Tri-NanoAb was also demonstrated through tumour tissue photography and measurement of tumour weight at the end of treatment (Fig. 4d,e). In addition, no obvious weight loss was observed in the mice after administration, indicating excellent tolerance to the dose used in the experiment (Supplementary Fig. 32).

After treatment with the control, FP-NA/Iso, mAbs Comb. or Tri-NanoAb, the entire tumour tissue from 4T1-bearing mice was subjected to RNA sequencing (RNA-seq), and the gene expression in the different treatment groups was determined based on the similarity of existing transcripts. Supplementary Fig. 33 shows a stacked bar plot of differentially expressed genes between the control, mAbs Comb. and Tri-NanoAb. To calculate tumour purity and immune cell infiltration, the ESTIMATE algorithm and ImmuCellAI-mouse were used to explore the tumour microenvironment[29]. The ESTIMATE algorithm was used to predict the overall tumour purity in these groups. The stromal score and immune score in the Tri-NanoAb group were higher than those in the other two groups; however, the opposite was true for tumour purity (Fig. 4f). The ImmuCellAI-mouse was used to predict the abundance of specific immune cell types or subtypes (Fig. 4g and Supplementary Fig. 34). The results for the seven main types of immune cell revealed an increased proportion of T cells after Tri-NanoAb treatment, particularly cytotoxic $CD8^+$ T cells, $CD4^+$ $T_H$ cells and NKT cells. The ratio of NK cells showed no obvious change. In addition, the enhanced infiltration of $CD8^+$ T cells in 4T1 tumours was confirmed by immunohistochemical staining and digital pathology microscope slide scanners (Supplementary Fig. 35). Then, to explore the mechanism associated, GSVA and gene set enrichment analysis (GSEA) of the Kyoto Encyclopedia of Genes and Genomes (KEGG) and GO terms were performed. GSVA enrichment analysis of KEGG gene sets was performed to further exploit the biological behaviours after different treatments. Gene sets associated with immune response such as the T cell receptor signalling pathway, NK cell-mediated cytotoxicity, $T_H1$ and $T_H2$ cell differentiation and chemokine signalling pathways were commonly upregulated, while the tricarboxylic acid cycle (TCA cycle) and cell cycle process was widely suppressed (Fig. 4h and Supplementary Fig. 36). GSEA was performed to compare the differences in the essential biological processes and pathways linked to the function of tumour-infiltrating immune cells between the Tri-NanoAb and mAbs Comb. groups. GSEA revealed that KEGG pathways were enriched in the antitumour immunity pathways (Fig. 4i). To investigate the significance and correlation of the curative effect between the Tri-NanoAb group and the mAbs Comb. treatment of individual tumours, GO enrichment analysis was performed to summarize the biological processes associated with immune cell function and tumour metabolism-related pathways. The activated signalling pathways were mainly related to adaptive immunity, whereas the suppressed signalling pathways were associated with DNA replication and cell proliferation (Fig. 4j). Protein–protein interaction network was constructed to analyse the connectivity of differentially expressed genes between mAbs Comb.- and Tri-NanoAb-treated 4T1 tumour tissues. *Tnf* and *Ifng* emerged as highly connected hub genes (potential key proteins) within this network, and the expression levels of *Tnf* and

**Fig. 3 | Tri-NanoAb increases T cell-mediated cytotoxicity in vitro and has better tumour enrichment ability without obvious biological toxicity.** **a**,**b**, Representative confocal images of B16F10 cells (**a**) and T cells (**b**) showed cell associations with mAbs Comb. and Tri-NanoAb after a 6 h incubation period. The cell membrane was stained with Calcein Violet 450 AM (blue); αPDL1, αPD1 and αNKG2A were labelled with AF647 (red), AF488 (green) and AF555 (purple), respectively. Scale bars, 10 μm and 2 μm, respectively. **c**, Representative confocal images showing the conjugations of $CD8^+$ T cells (red) on B16F10 tumour cells. B16F10 cells and DID-labelled $CD8^+$ T cells were co-incubated for 8 h in the presence of different treatments, and cell conjugations were detected after washing. Scale bars, 20 μm. **d**, The viability of B16F10-Luc cells was analysed by detecting luciferase activity. conc., concentration. Data are presented as mean ± s.d. ($n = 3$ biologically independent samples). **e**, The stacked bar plot illustrating differentially regulated gene expression from RNA-seq analysis between the control, mAbs Comb. and Tri-NanoAb treatment groups. Values are presented as $\log_2$ of tag counts ($n = 3$ biologically independent samples for the control group, $n = 4$ for mAbs Comb. and Tri-NanoAb treatment groups). **f**, GSVA of GO signalling pathway analysis in apoptosis and T cell function between the control, mAbs Comb. and Tri-NanoAb treatment groups ($n = 3$ biologically independent samples for the control group, $n = 4$ for mAbs Comb. and Tri-NanoAb treatment groups). **g**, Blood circulation half-life of fluorescent-labelled antibodies in the form of mAbs Comb. or Tri-NanoAb. Data are presented as mean ± s.d. ($n = 3$ biologically independent samples). **h**, IVIS imaging depicting the accumulation of Tri-NanoAb in orthotopic 4T1 tumours. **i**, Quantification of mAbs accumulation in tumour tissues. Data are presented as mean ± s.d. ($n = 3$ biologically independent samples). **j**, Enrichment of mAbs in tumour tissues. Scale bars, 50 μm. **k**–**n**, Toxicological analysis, ALT (**k**), AST (**l**), creatinine (**m**) and CK (**n**) levels, after treatment with control, FP-NA/Iso, mAbs Comb. and Tri-NanoAb. Data are presented as mean ± s.d. ($n = 6$ biologically independent samples). **o**, Representative H&E staining images of major organs in control, FP-NA/Iso, mAbs Comb. and Tri-NanoAb after 3 months of administration. Scale bars, 100 μm. The *P* values in **g** and **i** were generated using two-tailed Student's *t*-test. The *P* values in **k**–**n** were generated using one-way ANOVA with Tukey's post hoc test. NS ($P > 0.05$), $^*P < 0.05$; $^{**}P < 0.01$. For **a**–**c**, **j** and **o**, images were obtained from 3 biologically independent samples, yielding similar results, and a representative image was provided for each group. Panels **a** and **b** were created with BioRender.com under a CC-BY-NC-ND licence.

*Ifng* were much higher in the Tri-NanoAb group than in the mAbs Comb. group (Supplementary Fig. 37), which can supply the reason why Tri-NanoAb effectively regulates the tumour microenvironment and exerts potent antitumour effects. These data indicate that Tri-NanoAb could remarkably inhibit tumour growth in many ways, including by strengthening the function of T cells. Finally, the expression levels of genes correlated with immune-related adverse events (irEAs) were analysed to prove that the mAbs Comb. and Tri-NanoAb did not induce irEAs in mice at this dose[30,31] (Supplementary Fig. 38).

The tumour therapeutic efficacy of Bi-mAbs, Bi-NanoAbs, Tri-mAbs and Tri-NanoAb was then compared at the animal level (Supplementary Fig. 39). Evidently, Bi-NanoAbs outperform Bi-mAbs in tumour treatment, while Tri-NanoAb outperforms Tri-mAbs. The tumour treatment effect of Tri-NanoAb exceeds that of Bi-NanoAb. Remarkably, Tri-NanoAb exhibits an exceptionally potent antitumour efficacy in 4T1 tumours, with its possible mechanisms encompassing the following three facets. (1) Tri-NanoAb comprises two immunomodulatory antibodies (anti-mouse PD1 antibody and anti-mouse NKG2A antibody) that synergistically activate tumour-infiltrating T cells and promote their proliferation. (2) Tri-NanoAb can simultaneously recognize tumour cells and T cells, fostering enhanced interaction and physical proximity between them. This enables T cells to secrete cytotoxic granules (for example, granzyme B and perforin)

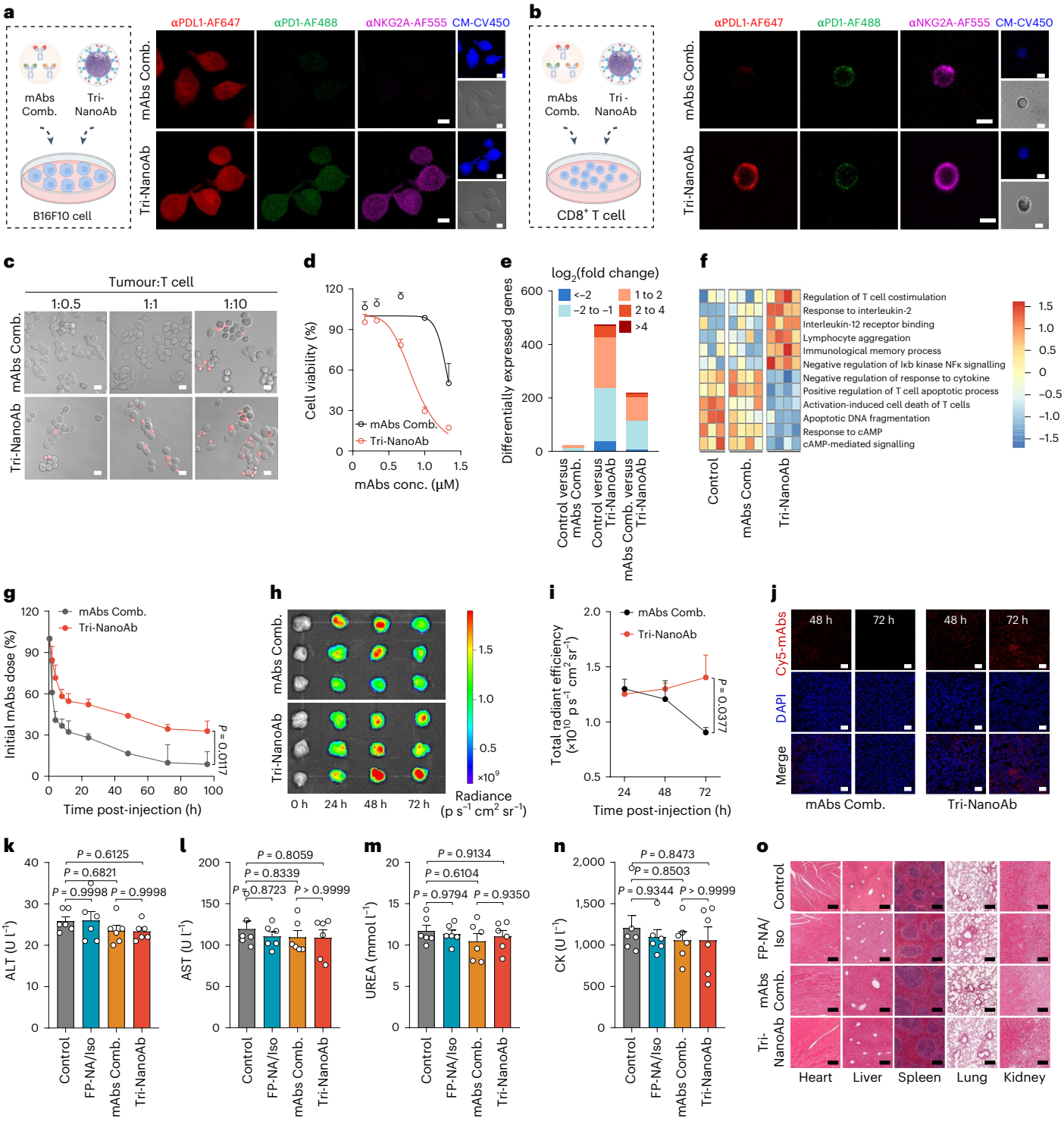

to induce apoptosis of neighbouring tumour cells. (3) Owing to its multivalent effect, Tri-NanoAb demonstrates increased affinity towards both tumour cells and T cells, facilitating more efficient enrichment within tumour tissues. Consequently, they effectively engage in immune modulation and exert antitumour activity.

The antitumour efficacy of the PDL1/PD1/NKG2A Tri-NanoAb was further assessed in a malignant melanoma model (Fig. 4k). C57BL/6 mice bearing firefly luciferase-labelled B16F10 tumours were treated with PBS, FP-NA/Iso, mAbs Comb. or Tri-NanoAb, and tumour progression was monitored based on bioluminescence signals using an in vivo imaging system (IVIS). As depicted in Fig. 4l, while tumours continued to proliferate in mice treated with FP-NA/Iso and were only partially restrained by the mAbs Comb., Tri-NanoAb extensively reduced the rates of tumour growth, as evidenced by weak bioluminescence signals. The remarkable superiority of the Tri-NanoAb in terms of its antitumour effects was confirmed by photographic evidence (Fig. 4m) and quantification of tumour tissue weight (Fig. 4n) at the end of treatment.

Tumour infiltration of immune cells was examined post-treatment using multicolour flow cytometry. The flow cytometry gating strategies for immune cells in tumour tissues are shown in Supplementary Figs. 40 and 41. As depicted in Fig. 4o, Tri-NanoAb treatment markedly increased the abundance of $CD3^+$ T cells in tumour tissues. Notably, the proportion of $CD8^+$ T cells among $CD3^+$ T cells and the ratio of $CD8^+CD69^+$ T cells was found to be higher than that in the control groups (Fig. 4p,q). Specifically, the ratio of $CD8^+/CD4^+$ T cells, which serves as an indicator for reversing the immunosuppressive microenvironment and predicting a favourable prognosis after treatment, was 2.8-, 2.9- and 1.3-fold higher than that of the control, FP-NA/Iso and mAbs Comb., respectively (Fig. 4r). Furthermore, a marked reduction of regulatory T ($T_{reg}$) cells, which are representative immunosuppressive immune cells, was observed in tumours treated with Tri-NanoAb (Fig. 4s). In addition, enhanced infiltration of $CD8^+$ T cells was confirmed by immunofluorescence staining and confocal microscopy (Fig. 4t). The indispensable role of T cells in the Tri-NanoAb-facilitated antitumour treatment was further corroborated by cell depletion experiments, as illustrated in Supplementary Fig. 42. αCD8-mediated depletion of $CD8^+$ T cells considerably compromised the therapeutic efficacy of Tri-NanoAb. In conclusion, it has been convincingly demonstrated that Tri-NanoAb effectively enhanced both the infiltration and proliferation of T cells while reversing the immunosuppressive microenvironment, which may account for its notably potent antitumour efficacy.

## FP-NA platform for constructing multiple multi-NanoAbs

After confirming the remarkable antitumour efficacy of FP-NA-based nano-antibody in mouse breast cancer and melanoma models, we further explored the potential of FP-NA as a versatile platform for constructing diverse bi-/multi-specific nano-antibodies to facilitate efficient cancer treatment. Numerous types of tumour cell exhibit overexpression of CD47, which possesses the capability to bind with the signal regulatory protein alpha (SIRPα) receptor on macrophages to transmit the 'do not eat me' signal[32]. Obstruction of the CD47-SIRPα signalling pathway can effectively eliminate the barrier hindering macrophages from engulfing these cells. In this study, anti-mouse CD47 antibody (clone MIAP301) and anti-mouse CSF1R antibody (clone AFS98), capable of recognizing CSF1R on macrophages, were immobilized onto FP-NA and used for constructing a bispecific nano-antibody (Bi-NanoAb) targeting both CD47 and CSF1R (Fig. 5a). The therapeutic efficacy of Bi-NanoAb, as shown in Fig. 5b, considerably surpassed that of the mAbs Comb. group. By monitoring the post-treatment survival period of the mice, as illustrated in Fig. 5c, we observed that after 49 days of tumour implantation, all mice in the control and mAbs Comb. groups perished, whereas the Bi-NanoAb treatment group exhibited an astonishing survival rate of 67%. The exceptional efficacy of Bi-NanoAb may be attributed to the enhanced interaction between macrophages and tumour cells, followed by engulfment of the tumour cells. Another example of FP-NA-based Bi-NanoAbs is CD3/CD19 Bi-NanoAb[33], which was meticulously engineered to augment the proficiency of $CD3^+$ T cells in recognizing and eradicating $CD19^+$ B-cell lymphoma (Fig. 5d). As anticipated, Bi-NanoAb demonstrated a remarkable antitumour effect in both the established systemic luciferase-enabled A20 model with tumour progression monitored using bioluminescence imaging (Fig. 5e) and subcutaneous A20 tumours measured by calipers (Fig. 5f).

As the representative FP-NA-based Tri-NanoAb, the therapeutic efficacy of PDL1/PD1/NKG2A Tri-NanoAb was further evaluated in both a spontaneous breast cancer model (Fig. 5g) and a lung metastasis model of melanoma (Fig. 5j). The mouse mammary tumour virus-polyoma middle tumour-antigen (MMTV-PyMT) model of breast cancer is widely used and well characterized[34,35]. MMTV-PyMT mice develop spontaneous mammary tumours that closely resemble the progression and morphology of human breast cancer[36]. Similar to the treatment effect in the 4T1 breast cancer model, the Tri-NanoAb group showed a more effective tumour inhibition effect than the mAbs Comb. group (Fig. 5h,i). In a lung metastasis model of melanoma, a comprehensive examination of the entire lung coupled with H&E staining confirmed a remarkable reduction in both the quantity and size of metastatic nodules within the mAbs Comb. group. Surprisingly, treatment with Tri-NanoAb almost completely abrogated lung metastasis of melanoma cells (Fig. 5k,l).

Survival rates for pancreatic cancer have shown minimal improvement over the past few decades (with only a mere 7% of diagnosed patients managing to survive beyond 5 years), rendering it one of the most formidable types of cancer for successful treatment[37,38]. Encouraged by the therapeutic efficacy demonstrated by the

**Fig. 4 | Tri-NanoAb exhibited superior antitumour efficacy in multiple mouse tumour models. a**, Schematic illustrating the treatment of the 4T1 orthotopic breast cancer model with PDL1/PD1/NKG2A Tri-NanoAb. **b**,**c**, Individual tumour growth curves (**b**) and average tumour growth rates (**c**) of 4T1 tumour-bearing mice. Data are presented as mean ± s.d. ($n = 7$ biologically independent mice per group). **d**, Tumour images collected at the treatment endpoints. **e**, Tumour weights after different treatments. Data are presented as mean ± s.d. ($n = 7$ biologically independent mice per group). **f**, Heat map showing the enrichment levels of immune infiltration characteristics obtained by the ESTIMATE algorithm (including stromal score, immune score, estimate score and tumour purity). **g**, The proportion of seven immune-associated infiltration cells. **h**, GSVA of KEGG signalling pathways in tumour-infiltrating immune cells and tumour cell metabolism between mAbs Comb.- and Tri-NanoAb-treated groups. **i**, The GSEA analysis of the five KEGG signalling pathways enrichment between mAbs Comb. and Tri-NanoAb groups. **j**, GO functional clustering of genes activated and downregulated for biological processes. NES, normalized enrichment score. **k**, Schematic illustrating the treatment of the B16F10-Luc subcutaneous tumour model with PDL1/PD1/NKG2A Tri-NanoAb. **l**, In vivo bioluminescence imaging of B16F10-Luc subcutaneous tumours in mice treated with mAbs Comb. or Tri-NanoAb. **m**, Tumour images collected at treatment endpoints. **n**, Tumour weights after different treatments. Data are presented as mean ± s.d. ($n = 6$ biologically independent mice per group). **o**–**s**, The number of $CD3^+$ T cells in per mg tumour tissues (**o**), the proportion of $CD8^+$ T cells in $CD3^+$ T cells (**p**), the proportion of $CD8^+CD69^+$ T cells in $CD3^+$ T cells (**q**), the fold change of $CD8^+/CD4^+$ T cells (**r**) and the percentage of $FoxP3^+$ $T_{reg}$ cells in $CD4^+$ T cells (**s**) were detected by multicolour flow cytometry. Data are presented as mean ± s.d. ($n = 5$ biologically independent samples). **t**, Representative fluorescence images of tumour lesions after staining with DAPI (blue) and AF647-labelled anti-mouse CD8 antibody (red). Scale bars, 100 μm. Images were obtained from 3 biologically independent samples, yielding similar results, and a representative image was provided for each group. The *P* values in **c** were generated using two-way ANOVA with Tukey's post hoc test. The *P* values in **n**–**s** were generated using one-way ANOVA with Tukey's post hoc test. NS ($P > 0.05$), *$P < 0.05$; **$P < 0.01$; ***$P < 0.001$; ****$P < 0.0001$. Panels **a**, **f** and **k** were created with BioRender.com under a CC-BY-NC-ND licence.

aforementioned FP-NA-based Bi- and Tri-NanoAb in multiple tumour models, we engineered a PDL1/PD1/NKG2A/4-1BB tetra-specific nano-antibody (Tetra-NanoAb) by anchoring four types of mAb onto FP-NA. We propose that this Tetra-NanoAb can effectively stimulate T cells and augment their cytotoxicity against pancreatic tumours. To evaluate its potential, we used a mouse orthotopic model featuring luciferase-expressing Pan02 cells (Pan02-Luc), which allowed us to conveniently monitor tumour progression in real time through non-invasive bioluminescence imaging (Fig. 5m). The treatment regimen involved administering an equal dose of antibody in control, mAbs Comb. and Tetra-NanoAb three times while monitoring tumour growth weekly using non-invasive techniques. Remarkably, the tumours in the group treated with the Tetra-NanoAb exhibited gradual shrinkage compared with those treated with mAbs Comb. Some showed signs of regrowth after initial reduction (Fig. 5n,o). Furthermore, direct observation via H&E staining confirmed a marked decrease in lesion size associated with pancreatic cancer in the group receiving Tetra-NanoAb treatment (Fig. 5p). Collectively, FP-NA can

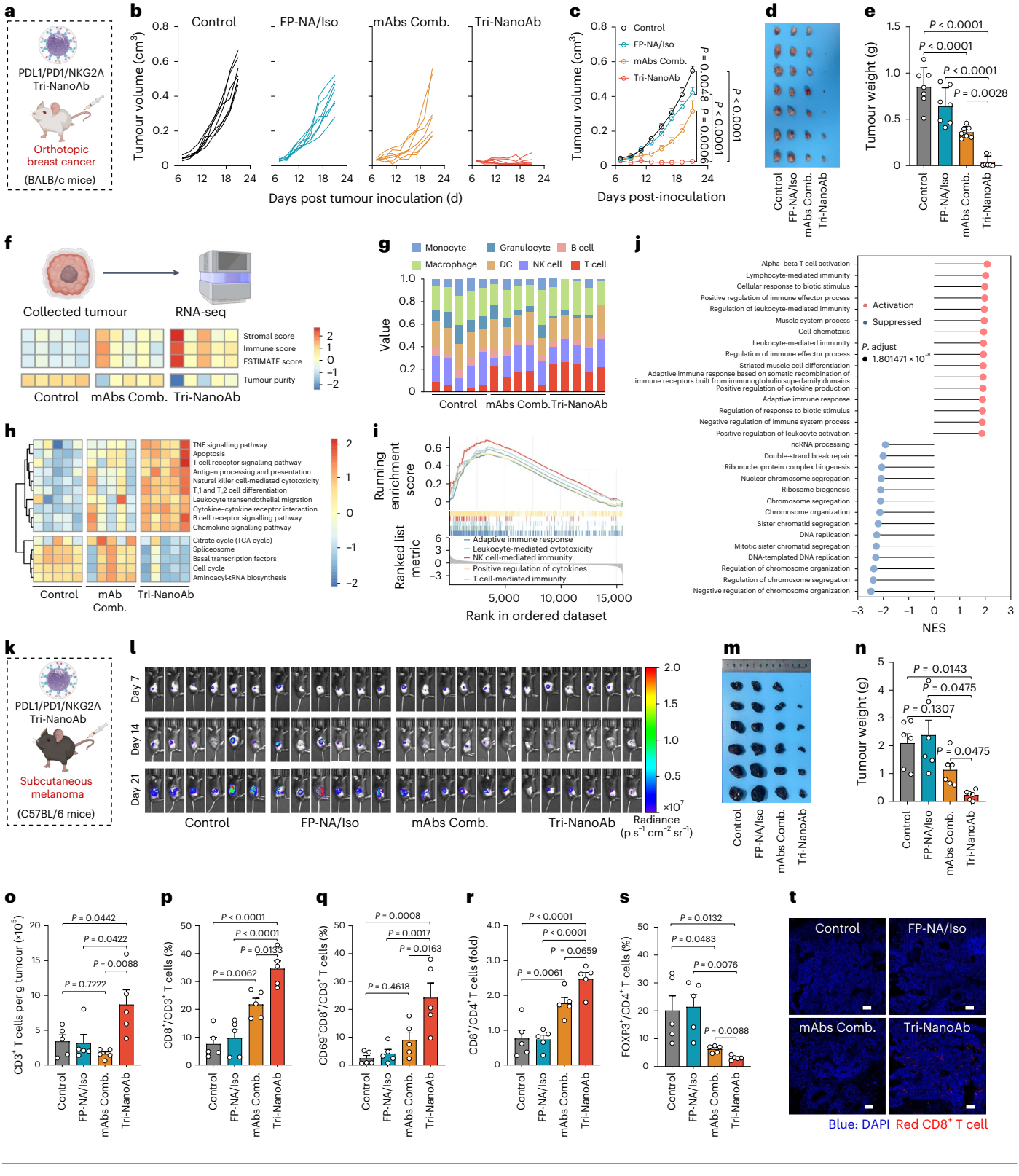

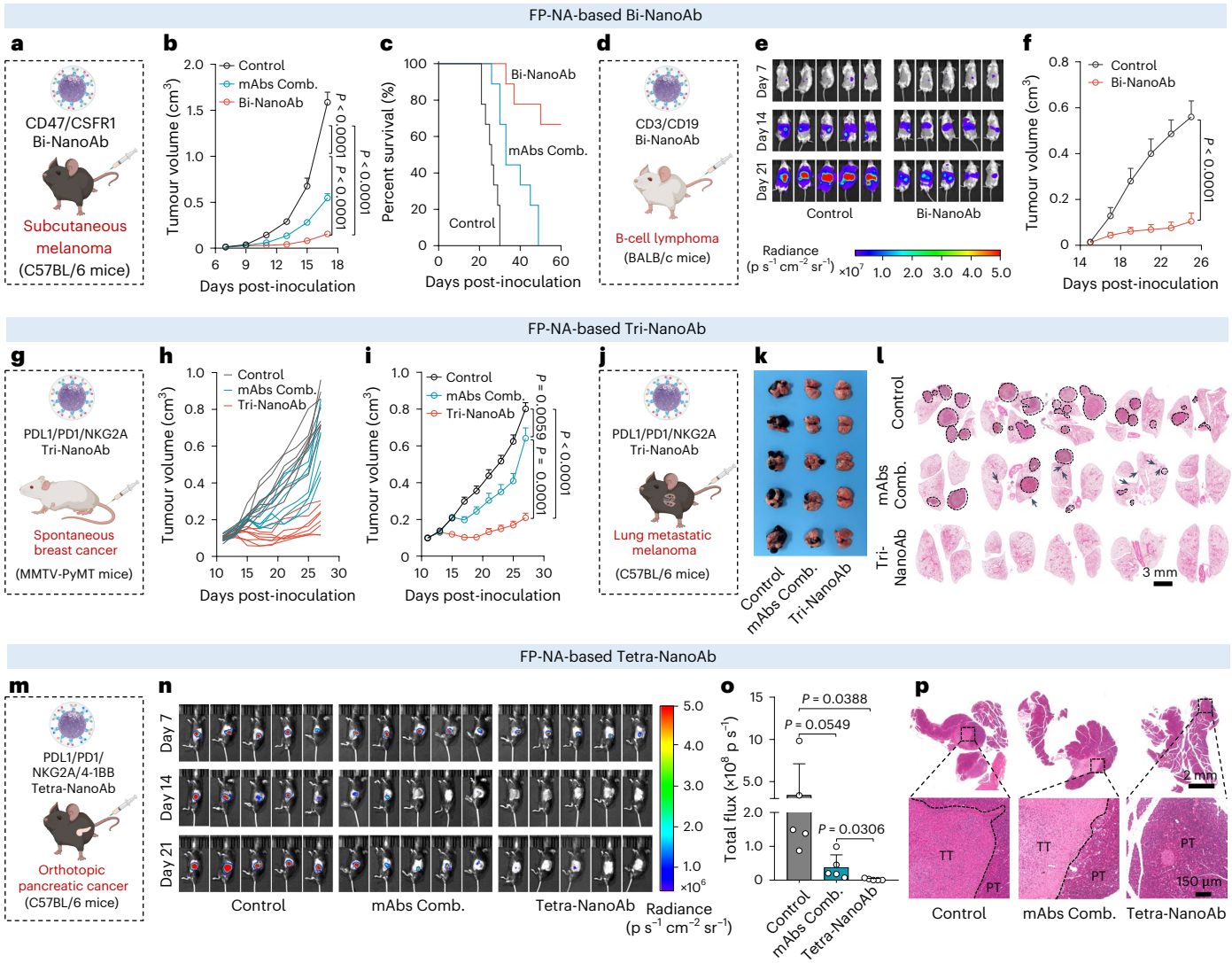


**Fig. 5 | FP-NA serves as a versatile platform for constructing multi-NanoAbs with efficient antitumour effects. a**, Schematic illustrating the treatment of the B16F10 subcutaneous melanoma model with CD47/CSF1R Bi-NanoAb. **b**,**c**, Average tumour growth rates (**b**) and survival curves (**c**) of B16F10 tumours in different groups. Data are presented as mean ± s.d. ($n = 9$ biologically independent mice per group). **d**, Schematic illustrating the treatment of systemic and subcutaneous A20-Luc B-cell lymphoma models with CD3/CD19 Bi-NanoAb. **e**, In vivo bioluminescence imaging of A20-Luc B-cell lymphoma in mice receiving mAbs Comb. or Bi-NanoAb treatments. $n = 5$ biologically independent mice per group. **f**, Average tumour growth rates of subcutaneous A20 tumour-bearing mice. Data are presented as mean ± s.d. ($n = 7$ biologically independent mice per group). **g**, Schematic illustrating the MMTV-PyMT spontaneous breast tumour model treatment with PDL1/PD1/NKG2A Tri-NanoAb. **h**,**i**, Individual tumour growth curves (**h**) and average tumour growth rates (**i**) of MMTV-PyMT tumour-bearing mice. Data are presented as mean ± s.d. ($n = 8$ biologically independent mice per group). **j**, Schematic illustrating the treatment of the B16F10-Luc lung metastatic melanoma tumour model with Tri-NanoAb (αPDL1, αPD1 and αNKG2A) ($n = 5$ biologically independent mice per group). **k**, Lung tissue images collected at treatment endpoints. **l**, Representative H&E images of lung tissues. **m**, Schematic illustrating the treatment of the Pan02-Luc orthotopic pancreatic tumour model with PDL1/PD1/NKG2A/4-1BB Tetra-NanoAb ($n = 5$ biologically independent mice per group). **n**, In vivo bioluminescence imaging of Pan02 orthotopic pancreatic tumours receiving mAbs Comb. or Tetra-NanoAb treatments. **o**, Quantification of total bioluminescence signals in tumour tissues. Data are presented as mean ± s.d. ($n = 5$ biologically independent samples per group). **p**, Representative H&E images of pancreatic tissue. For **c**, statistical significance was calculated using the log-rank (Mantel–Cox) test. The $P$ values in **b**, **f** and **i** were generated using two-way ANOVA with Tukey's post hoc test. The $P$ values in **o** were generated using two-tailed Student's $t$-test. NS ($P > 0.05$), $^*P < 0.05$; $^{**}P < 0.01$; $^{***}P < 0.001$; $^{****}P < 0.0001$. For **p**, images were obtained from 5 biologically independent samples, yielding similar results, and a representative image was provided for each group. Panels **a**, **d**, **g**, **j** and **m** were created with BioRender.com under a CC-BY-NC-ND licence.

serve as a versatile mAb immobilization platform and facilitate the convenient and efficient construction of a diverse array of multi-NanoAbs through the meticulous selection of mAb combinations.

## Clinical translational prospects of FP-NA and multi-NanoAbs

FP-NA could serve as a versatile mAb immobilization platform and facilitate the convenient and efficient construction of a diverse array of multi-NanoAbs through a meticulous selection of mAb combinations. Given that the potent antitumour effects of FP-NA-based multi-NanoAbs have only been validated in mouse tumour models, we aim to further explore the translational potential of FP-NA by developing a humanized version incorporating fusion proteins (hFcγR1–HSA) composed of human FcγR1 extracellular segments and human serum albumin (HSA) (Fig. 6a). Moreover, we comprehensively investigated the scale-up process for humanized FP-NA (hFP-NA) production and evaluated the therapeutic efficacy of nano-antibodies in humanized immune system mouse models[39]. The expression of hFcγR1–HSA was achieved through a mammalian protein expression

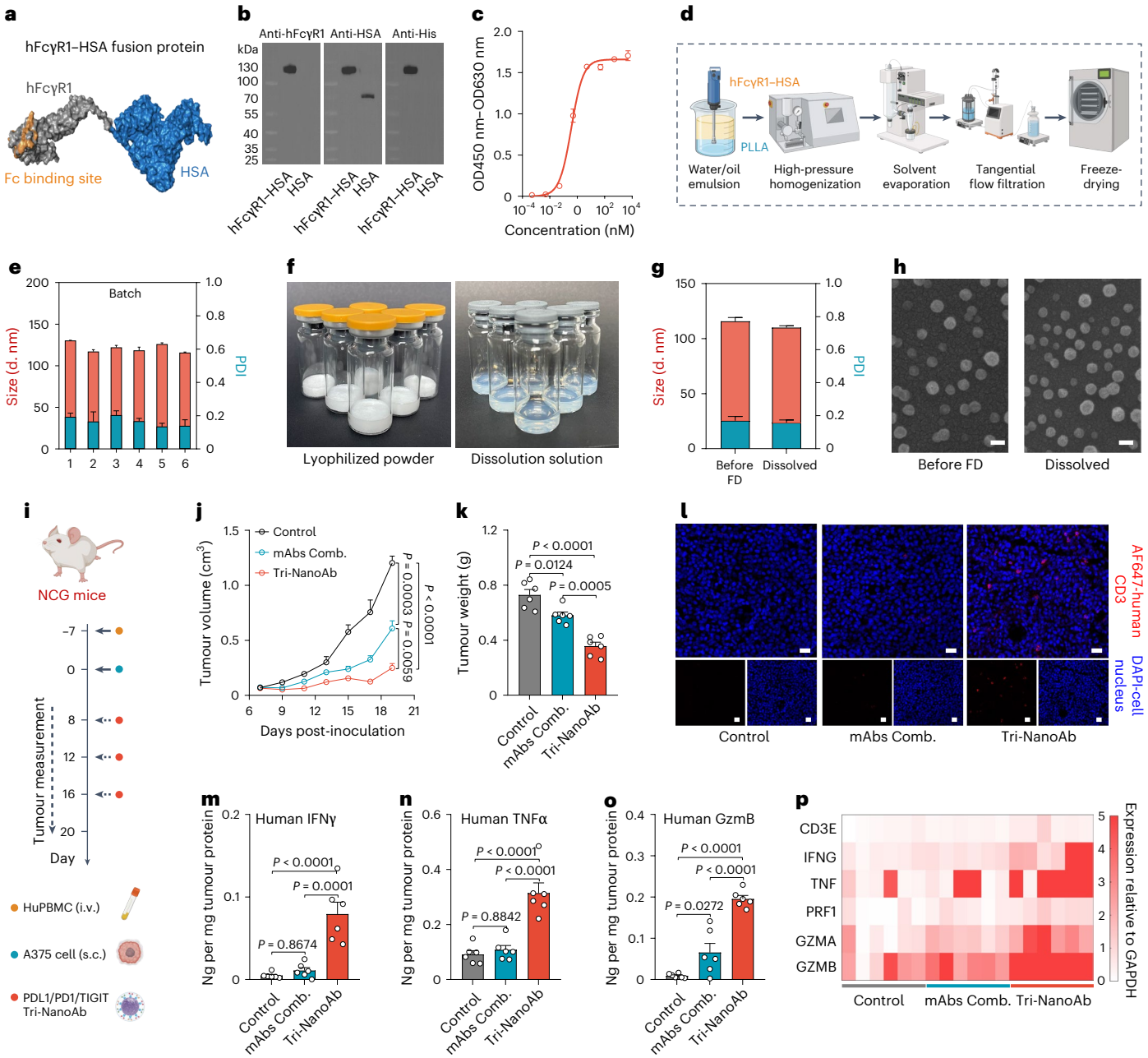


**Fig. 6 | Humanized FP-NA has clinical prospects and Tri-NanoAb exhibits favourable antitumour efficacy in the Hu-PBMC humanized mouse model.** **a**, 3D structure prediction for hFcγR1–HSA fusion protein. **b**, Western blotting analyses of the main components (hFcγR1, HSA and His tag) of hFcγR1–HSA. **c**, The binding of αhPDL1 to hFcγR1–HSA by single-antigen captured ELISA at the indicated concentration. Data are presented as mean ± s.d. ($n = 3$ biologically independent samples). **d**, Schematic illustrating the pilot production pipeline of humanized FP-NA. **e**, The average hydrodynamic size and PDI of hFP-NA were produced in multiple batches. Data are presented as mean ± s.d. ($n = 3$ biologically independent samples). **f**, The appearance of lyophilized powder (left) and dissolution solution (right). The lyophilized powder was obtained from three batches, yielding similar results. **g**, Average hydrodynamic size and PDI of humanized FP-NAs before and after freeze-drying. Data are presented as mean ± s.d. ($n = 3$ biologically independent samples). **h**, Representative SEM images of humanized FP-NAs before and after freeze-drying. Scale bars, 100 nm. **i**, Experimental protocol for the Hu-PBMC humanized xenogeneic melanoma model used in **j**–**p**. i.v., intravenously; s.c., subcutaneously. **j**,**k**, Average tumour growth curves (**j**) and tumour weight (**k**) measured from treatment endpoints of A375 tumour-bearing mice in different groups. Data are presented as mean ± s.d. ($n = 6$ biologically independent mice per group). **l**, Representative fluorescence images of tumour lesions after staining with DAPI (blue) and AF647 anti-human CD3 antibody (red). Scale bars, 20 μm. **m**–**o**, The level of human IFNγ (**m**), human TNFα (**n**) and human granzyme B (**o**) in treated A375 tumours was examined by ELISA. Data are presented as mean ± s.d. ($n = 6$ biologically independent samples). **p**, Expression of human T cell function-related genes in the A375 tumours after different treatments examined by qPCR. Data are presented as mean ± s.d. ($n = 6$ biologically independent samples). The $P$ values in **j** were generated using two-tailed Student's $t$-test. The $P$ values in **k** and **m**–**o** were generated using one-way ANOVA with Tukey's post hoc test. NS ($P > 0.05$), $^{*}P < 0.05$; $^{**}P < 0.01$; $^{***}P < 0.001$; $^{****}P < 0.0001$. For **b**, **h** and **l**, images were obtained from 3 biologically independent samples, yielding similar results, and a representative image was provided for each group. Panels **d** and **i** were created with BioRender.com under a CC-BY-NC-ND licence.

system (CHO-K1Q cells), and its pre-designed functional components as well as affinity towards the Fc fragment of human IgG1 antibody were evaluated via western blot (Fig. 6b) and ELISA (Fig. 6c), respectively.

The pilot production pipeline for hFP-NA was meticulously designed to encompass pre-emulsification, homogenization, solvent removal, purification, sterile filtration and lyophilization (Fig. 6d). We used an orthogonal design of experiments methodology to discern the most efficacious hFP-NA formulations via library screening with various critical material attributes (including the protein concentration, protein/PLLA weight ratio and oil/water volume ratio, among others) and critical process parameters (including dispersion speed of disperser and pressure and cycles of homogenization, among others) as input variables and critical quality attributes (including size, PDI, protein entrapment efficiency and loading capacity, among others) as output key quality indicators. The average hydrodynamic size of hFP-NA across multiple production batches was settled in the range of 110–130 nm, with a PDI of less than 0.23 (Fig. 6e). The freeze-dried product exhibits a flawless appearance, as depicted in Fig. 6f, forming a dense and porous block structure with excellent solubility. The particle size and PDI of hFP-NA remained unaltered after freeze-drying (Fig. 6g). SEM was used to characterize the morphology of hFP-NAs before and after freeze-drying, confirming the absence of any substantial alterations (Fig. 6h).

Finally, we fabricated a PDL1/PD1/TIGIT Tri-NanoAb by immobilizing three types of humanized mAb (αPDL1, αPD1 and αTIGIT) onto dissolved freeze-dried hFP-NA. We evaluated its antitumour effect in a subcutaneous A375 human melanoma xenograft model using humanized NCG mice with peripheral blood mononuclear cells (PBMCs). As depicted in Fig. 6i, human PMBCs were intravenously (i.v.) administered 7 days before tumour inoculation. Starting from day 8 post-A375 inoculation subcutaneously (s.c.), tumour-bearing NCG mice were treated 3 times (at 3-day intervals) with IgG1 control, mAbs Comb. (αPDL1, αPD1 and αTIGIT) or Tri-NanoAb, and tumour progression was monitored every other day. We monitored the changes in the proportion of human immune cells in the blood of the hu-PBMC humanized mouse model (Supplementary Fig. 43). The tumours in the group treated with Tri-NanoAb exhibited gradual shrinkage compared with those treated with mAbs Comb., as evidenced by the tumour growth curve and tumour weight calculation post-treatment (Fig. 6j,k). Immunofluorescence results demonstrated that Tri-NanoAb treatment considerably increased the infiltration of $CD3^+$ T cells into tumour tissues compared with the control and mAbs Comb. groups (Fig. 6l), respectively. As expected, higher levels of tumour-killing-related cytokines, such as active ingredeint-γ (IFNγ), tumour necrosis factor-α (TNFα) and granzyme B (GzmB), were detected in the Tri-NanoAb-treated tumour tissue (Fig. 6m–o). The qPCR data confirmed that treatment with Tri-NanoAb enhanced T cell infiltration into tumours and augmented their cytotoxicity (Fig. 6p).

## Discussion

Although the application of immune checkpoint inhibitors in tumour immunotherapy is widespread, there remains a need for substantial improvement in their antitumour efficacy and clinical response rate[40–42]. In recent years, multi-specific antibodies, capable of simultaneously recognizing two or more antigen epitopes, have garnered increasing attention as an effective strategy to overcome the issue of insufficient potency observed with mAbs[43]. Multi-mAbs possess unique attributes, including multivalence characteristics, immune cell redirection functionality and synchronized spatiotemporal signalling regulation, which enable them to achieve enhanced therapeutic effects[44,45]. However, their structural design complexity and production process have considerably escalated compared with mAbs[5]. By immobilizing multiple mAbs on nanocarriers' surfaces, it becomes possible to mimic multi-Abs' functions while achieving multivalent, multi-specific and multi-functional attributes[46,47]. It is worth noting that a combination of nanoparticles conjugated with distinct functional antibodies (where each nanoparticle is conjugated with one type of antibody) can also modulate immune cell function; however, they cannot serve as a 'bridge' between immune cells and tumour cells and facilitate their interactions, resulting in limited therapeutic effect. Nevertheless, there is an urgent need to investigate and develop a nanoplatform for the facile preparation of multi-NanoAbs while overcoming the bottlenecks posed by chemically bonded antibody molecules that may compromise drug activity.

The Fc receptors are a family of cell surface proteins that specifically bind to the Fc fragment of antibodies and induce immune responses[48]. Among these receptors, FcγR1 predominantly expressed in macrophages and monocytes exhibits robust binding affinity towards IgG1/4 antibodies in humans and IgG2a/2b antibodies in mice[18,49]. Drawing inspiration from this phenomenon, we propose to explore the potential of FcγR1 for constructing nanoplatforms for mAb immobilization. SA, as the most abundant protein in plasma, possesses several desirable characteristics, including exceptional biocompatibility and low immunogenicity[50]. Owing to these properties, it has found extensive application in the development of drug carriers (for example, active ingr., an albumin-bound active ingredient ). A molecular-level analysis of SA's structure reveals its ability to bind multiple ligands, including LCFA[19]. This unique feature presents an opportunity for albumin and hydrophobic polymers to assemble into stable particles[51]. In this study, we successfully engineered a nanoplatform for immobilizing mAbs by using the fusion protein of FcγR1–SA along with hydrophobic polymers using ultrasonic emulsification and high-pressure homogenization techniques. The existence of FcγR1 on the particle surface confers exceptional binding capabilities to mAbs drugs, leading us to christen this nanoplatform as FP-NA. Compared with our previous nanosystem, FP-NA holds several improvements and advantages. The composition is simplified, requiring only fusion protein FcγR1–SA and PLLA without the need for anti-Fc antibody. It also circumvents intricate chemical reactions such as anti-Fc antibody oxidation and conjugation. There is no necessity for reagent application (for example, $NaIO_4$ and $NaBH_4$) or corresponding purification steps. Finally, it is suitable for large-scale preparation through a streamlined one-step process. Serving as a versatile platform, FP-NA allows for the convenient, efficient and controlled construction of multi-NanoAbs. We have successfully fabricated a variety of bi-, tri- and tetra-specific NanoAbs and demonstrated exceptional antitumour efficacy across a diverse range of tumour models, including orthotopic and spontaneous breast cancer, melanoma and orthotopic pancreatic cancer models. Furthermore, important milestones have been reached in the development of the humanized FP-NA construction and the scaling up of the manufacturing process. These advances allow us to validate the antitumour efficacy of multi-NanoAbs in humanized mouse models.

It is widely acknowledged that the use of cost-effective raw materials and optimization of their use rate holds paramount importance in the construction of nano-delivery systems. Consequently, several strategies can be used to enhance the efficiency of FcγR1–SA in FP-NA construction and further reduce the expenses associated with its production. First, by optimizing various parameters in FP-NA preparation, including meticulous polymer selection (for example, PLLA and PLGA), fine-tuning polymer molecular weight, and carefully adjusting weight and volume ratios between polymer and FcγR1–SA, we anticipate an enhancement in the assembly efficiency of FcγR1–SA. In addition, optimal parameter settings of high-pressure homogenizer (for example, pressure and time) may also increase the assembly efficiency of FcγR1–SA. Second, successful recovery of unassembled FcγR1–SA is expected to be achieved through hollow fibre tangential flow filtration. By regulating the molecular weight cut-offs of fibre filter membranes, it is possible to separate the unassembled fusion protein FcγR1–SA from the constructed FP-NA and recover it for reuse. Third, high-throughput screening techniques enable the selection of cell

clones and the construction of stable cell lines with higher expression yields. In addition, implementing high-density cultivation of cells using bioreactors could produce more recombinant protein. These are commonly used methods in industry to improve recombinant protein yields that can assist us in obtaining substantial amounts at reduced costs.

Meanwhile, we acknowledge the imperative for extensive investigation of the in vivo metabolic behaviour, biosafety and antitumour mechanisms of multi-NanoAbs. Furthermore, we remain steadfast in our commitment to optimizing the scale-up and manufacturing processes for FP-NA and multi-NanoAbs while actively promoting preclinical trials. Considering that there are no insurmountable barriers to the application of FP-NA and multi-NanoAbs in terms of excipient safety, excipient availability and preparation process maturity, we firmly believe that FP-NA will find diverse applications in the biomedical field. For example, the FP-NA offers an approach to constructing tetra- or penta-specific antibodies whose production using conventional antibody engineering techniques is an obstacle. Highly heterogeneous diffuse B-cell lymphoma is expected to be completely cured by CD3/CD28/CD19/CD20/CD22 Penta-NanoAbs[52]. Similarly, IL1/IL6/TNFα/IFNγ Tetra-NanoAbs capable of simultaneously neutralizing multiple types of cytokine provide a strategic solution for relieving cytokine release syndrome[53]. Another potential application of FP-NA is to enable high-throughput screening of multi-Abs or multi-NanoAbs combinatorial targets. By harnessing FP-NA and a repertoire of modulatory mAbs, it becomes incredibly convenient to construct a library of multi-NanoAbs with different target combinations. Furthermore, by the PBMC–tumour cell co-culture system, arrays of multi-NanoAbs with exceptionally potent antitumour effects and innovative mechanisms can be meticulously screened, thereby expediting the development of antibody–drug.

In summary, we have devised FP-NA using two components with exceptional biosafety for immobilizing mAbs and constructing multi-NanoAbs. We effectively tackled the challenges associated with the clinical translation of previously developed multi-NanoAbs, which were hindered by intricate fabrication procedures and concerns regarding carrier biosafety. With the aid of FP-NA, it is now possible to conveniently construct multi-NanoAbs with four, five or even more specificities—a feat that was previously difficult to achieve with antibody engineering techniques. The use of FP-NA and multi-NanoAbs holds immense potential in expanding the application scope of antibody drugs for various diseases, including, but not limited to, tumours.

# Methods

## Materials and reagents

Poly(L-lactide) (HO-PLLA-COOH, abbreviated as PLLA, $\bar{M}_w$: 1.5 kDa, 7.2 kDa, 19 kDa, 64 kDa, 100 kDa, 130 kDa, 159 kDa, 240 kDa, 600 kDa and 1,100 kDa) was purchased from Jinan Daigang Biomaterial. Anti-mouse PD1 (clone RMP1-14), anti-mouse NKG2A/C/E (clone 20D5), anti-mouse 4-1BB (clone 3H3), anti-mouse CSF1R (clone AFS98), anti-mouse CD47 (clone MIAP301), anti-mouse CD3 (clone KT30), anti-mouse CD8α (clone 53-6.7), anti-mouse 4-1BB (clone 3H3), anti-mouse 4-1BBL (clone TKS-1), anti-mouse TIM-3 (clone RMT3-23), anti-mouse NK1.1 (clone PK136) and IgG2a isotype control (clone 2A3) were purchased from Bio X Cell. The anti-mouse PDL1 (clone MIH6) antibody was purchased from BioLegend. Recombinant mouse FcγR1, PDL1, PD1 and NKG2A protein were obtained from Sino Biological. Anti-mouse FcγR1 antibody (clone 27), anti-human FcγR1 antibody (clone EPR4623), anti-mouse/human albumin antibody (clone EPR20195) and anti-6× His tag antibody (clone HIS.H8) were sourced from Abcam. All antibodies used for flow cytometry assays were purchased from BioLegend. Sulfo-Cy5 NHS ester, Sulfo-Cy3 NHS ester and Biotin NHS ester were purchased from J&K Scientific. Alexa Fluor 488 NHS ester, Alexa Fluor 555 NHS ester, Alexa Fluor 647 NHS ester and Calcein Violet 450 AM were purchased from Thermo Fisher Scientific. DID dye and Cell Counting Kit-8 were acquired from Beyotime Biotech. Cells and antibodies were labelled according to the manufacturer's protocol.

## Cell lines

B16F10 mouse melanoma cells, 4T1 mouse breast cancer cells, Pan02 mouse pancreatic cancer cells, A20 mouse B-cell lymphoma cells and A375 human melanoma cells were obtained from the American Type Culture Collection (ATCC). HEK293F was obtained from FuHeng BioLogy. CHOK1Q was obtained from QuaCell Biotechnology. For bioluminescence imaging, a construct expressing firefly luciferase (Luc) was introduced into B16F10, Pan02 and A20 cells via lentiviral transduction. All tumour cells were cultured in Dulbecco's modified Eagle's medium (DMEM) (Gibco) or RPMI medium 1640 (Gibco) supplemented with 10% FBS (ExCell Bio) and 1% active ingredient/active ingredient (Gibco). All cells were kept in a 37 °C incubator supplied with 5% $CO_2$. All cell lines tested negative for *Mycoplasma* using a DNA-based polymerase chain reaction (PCR) (Beyotime Biotech).

## Mice

Male C57BL/6 and female BALB/c and C57BL/6 (6–8 weeks old) mice were purchased from Hunan Silaike Jingda Laboratory Animal Technology. Friend virus B-type (FVB) mice were purchased from Beijing Vital River Lab Animal Technology. NOD/ShiLtJGpt-*Prkdc*$^{em26Cd52}$*Il2r*$^{gem26Cd22}$/Gpt (NCG, strain number T001475) were purchased from GemPharmatech. MMTV-PyVT (FVB/N-Tg(MMTV-PyVT)634Mul/J) transgenic mice were generously gifted by Z. X. Lian from Guangdong Provincial People's Hospital. All mice were maintained at the Laboratory Animal Research Center of the South China University of Technology (SCUT) in a specific pathogen-free environment. All mice were housed in pathogen-free conditions and maintained in a room with controlled temperature (~22 °C) and humidity (50 ± 15%) under a 12 h/12 h light/dark cycle. All animal experiments were approved by the Animal Care and Use Committee of the SCUT, and efforts were made to minimize the pain caused by the experiments.

## Characterization of mFcγR1–MSA and hFcγR1–HSA

Western blotting, LC-MS/MS and ELISA were used to characterize the fusion proteins. The concentrations of purified proteins were measured using a Pierce BCA protein assay kit (Thermo Fisher Scientific). Western blotting assay was conducted by a standard protocol with the following antibodies: anti-mouse FcγR1 antibody (clone 27, 1:5,000 dilution), anti-mouse/human albumin antibody (clone EPR20195, 1:5,000 dilution), anti-6× His tag antibody (clone HIS.H8, 1:5,000 dilution), anti-human FcγR1 antibody (clone EPR4623, 1:5,000 dilution), goat anti-rabbit IgG H&L (HRP) (polyclone, 1:10,000 dilution) and goat anti-mouse IgG H&L (HRP) (polyclone, 1:10,000 dilution). LC-MS/MS analysis was performed by Sangon Biotech.

To assess the binding kinetics of mFcγR1–MSA to IgG2a antibodies, ELISA plates (Corning) were coated with 100 µl (1 µg ml$^{-1}$) of mAbs for 12 h at 4 °C. Subsequently, a non-protein-blocking solution (Sangon Biotech) was added and incubated for 2 h at room temperature. A series of concentrations of mFcγR1–MSA were then added and incubated for 1 h at 37 °C. After the washing steps, the HRP-conjugated anti-albumin antibody (clone #101, 100 µl, 1 µg ml$^{-1}$) was added and incubated for 45 min at room temperature. This was followed by the addition of a solution containing 3,3′,5,5′-tetramethylbenzidine (TMB) (100 µl). After a further incubation period of 12 min, the reaction was stopped using a stop solution. The absorbance at 450 nm and 630 nm in each well was measured using Tecan Infinite M200PRO with TECAN iControl (version 2.0). The dissociation constant ($K_d$) was determined by plotting normalized absorbance values against the concentrations of mFcγR1–MSA using GraphPad Prism version 8.0 (GraphPad Software).

### Preparation and characterization of FP-NA

FP-NA was prepared by ultrasonic emulsification (small scale) and high-pressure homogenization (large scale). In brief, an aqueous solution of FcγR1–SA (10 mg ml$^{-1}$) and PLLA dissolved in chloroform (10 mg ml$^{-1}$) were ultrasonically mixed at a volume ratio of 5:1 over an ice bath using an ultrasonic processor (Sonics & Materials), forming an emulsion. Demulsification and removal of organic solvents were performed using a rotary evaporator (IKA). The obtained FP-NA was then purified by ultracentrifugation at 20,000 × *g* for 90 min and resuspended in 1× PBS, and stored at 4 °C. For large-scale production, an aqueous solution of FcγR1–SA (5 mg ml$^{-1}$) and PLLA dissolved in chloroform (10 mg ml$^{-1}$) were primarily mixed at a volume ratio of 10:1 over an ice bath using a high-speed disperser at 10,000 rpm for 60 s (T18 digital ULTRA-TURRAX, IKA), forming a crude emulsion, which was further homogenized under a high-pressure microfluidizer (Nano-Genizer 30 K, Genizer) at 12,000 psi for 4 cycles. Demulsification and removal of organic solvents were performed using a rotary evaporator (IKA). The obtained FP-NA was then purified using a Repligen KrosFlo KR2i TFF system with hollow fibre filters, and finally sterile-filtered with 0.22 μm PES filters (Millipore). The obtained FP-NA solution in 1× PBS was lyophilized using a freeze-dryer (FTS LyoStar 3, SP Scientific) by adding trehalose with a final concentration of 10% (w/v) as the cryoprotectant. Samples were frozen at −45 °C for 3 h, followed by a primary drying cycle at −31 °C/55 mTorr for 36 h and a secondary drying cycle at 10 °C/55 mTorr for 10 h, respectively. At the end of the freeze-drying process, vials were backfilled with nitrogen, capped and stored at 4 °C.

The FP-NA morphology was observed using a scanning electron microscope (SEM, Merlin, Zeiss). The hydrodynamic size, PDI and zeta potential of FP-NA were measured using a Zetasizer Nano ZSE instrument (Malvern Panalytical) with Malvern Zetasizer Software v7.12. The loading efficiency of mFcγR1–MSA was quantified by HPLC equipped with XBridge BEH200Å SEC 3.5 μm, 7.8 × 150 mm column (Waters) and Kjeldahl apparatus (Hanon). The Alexa Fluor 488-labelled mFcγR1–MSA was obtained according to the manufacturer's instructions, while RhoB (rhodamine B) was coupled to PLLA by condensation reaction. $FP\text{-}NA_{AF488\text{-}mFc\gamma R1\text{-}MSA/RhoB\text{-}PLLA}$ were subsequently prepared using the aforementioned methods for direct visualization of the assembly between mFcγR1–MSA and PLLA. Images were acquired using a stochastic optical reconstruction microscope (Abbelight) equipped with 488 nm and 532 nm lasers and NEO software V2.15.2 (Abbelight). The assembly of mFcγR1–MSA and PLLA was further validated via Flow NanoAnalyzer (NanoFCM) validated via Flow NanoAnalyzer with NanoFCM Profession V2.0. To assess in vitro stability, we measured the hydrodynamic size and PDI of FP-NA in PBS and DMEM containing 10% FBS at 37 °C for 8 days using a Zetasizer Nano ZSE instrument (Malvern Panalytical).

### Construction and characterization of FP-NA-based nano-antibodies

The FP-NA is designed to possess the capability of immobilizing mAbs with conserved Fc fragments through FcγR1 on its surface; the specific interaction between FP-NA and mAbs is detected by a MicroCal PEAQ-ITC system (Malvern Panalytical) with MicroCal PEAQ-ITC control software (version 1.1). In brief, a titration needle was used to drop the mAbs (5 mg ml$^{-1}$) into a sample pool containing FP-NA (1 mg ml$^{-1}$) solution, and the thermodynamic parameters during the titration process were recorded. Nanoparticles ($NP_{MSA/PLLA}$) engineered using MSA and PLLA served as controls.

The immobilization capacity of FP-NA for mAb was assessed via ELISA, using αPDL1 as an illustrative exemplification. In brief, 100 μl of recombinant PDL1 protein (rPDL1) at a concentration of 0.5 μg ml$^{-1}$ in 0.05 M carbonate buffer at pH 9.6 was added to a 96-well ELISA plate and incubated at 4 °C for a duration of 12 h. After washing the plate three times with PBST to remove unbound antigens, a non-protein-blocking solution (Sangon Biotech) was added and incubated for 2 h at room temperature. FP-NA was incubated with αPDL1 at varying mass ratios of mFcγR1–MSA to antibody for 16 h at 4 °C. The resulting FP-NA/αPDL1 nanocomplex was collected via centrifugation at 20,000 × *g* for 90 min, and the supernatant was transferred to rPDL1-coated wells. The wells were then incubated for 1 h at 37 °C before being rewashed. HRP-conjugated anti-rat IgG antibody (100 μl, 1 μg ml$^{-1}$) was added and incubated for an additional 45 min at room temperature before the addition of a solution containing TMB (100 μl). After a further 12 min incubation period, the reaction was stopped by adding a stop solution. The absorbance intensity was measured using Tecan Infinite M200PRO with TECAN iControl (version 2.0) at 450 nm and 630 nm.

FA-NA-bound mAbs were quantified using the following formula:

$$\text{Bound mAbs} = \text{total mAbs} - \text{unbound antibodies in solution}$$

To determine the average quantity of mAbs immobilized on each FP-NA, FITC-labelled mAbs were incubated with FP-NA at different mass ratios of mAbs and mFcγR1–MSA in FP-NA (wherein the mFcγR1–MSA content in FP-NAs was examined by HPLC and Kjeldahl nitrogen analyser). The fluorescence intensity of mAbs bound to FP-NAs was subsequently detected using the NanoFCM NanoAnalyzer. Co-incubation of mAbs and FP-NA was carried out with a mass ratio of mAbs to mFcγR1–MSA being 1:10 while maintaining a final concentration of 100 μg ml$^{-1}$ for the mAbs solution. The average NanoAb concentration was examined by NTA. Valence can be calculated using the following formula:

$$\text{Valence} = \frac{\text{concentration (mAb)}}{M_w\,\text{(mAb)}} \times N_A \div \text{concentration (NP)}$$

where $N_A$ is Avogadro's constant (~$6.02 \times 10^{23}$) and $M_w$(mAb) is the molecular weight of mAbs (~150 kDa).

αPDL1, αPD1 and αNKG2A were labelled with Alexa Fluor 488, Alexa Fluor 555 and Alexa Fluor 647, respectively, according to the manufacturer's instructions. Three types of labelled mAb (in a mass ratio of 1:1:1) were co-incubated with FP-NA using the mass ratio of mFcγR1–MSA to mAbs at 10:1. After incubation for 2 h at room temperature, PDL1/PD1/NKG2A Tri-NanoAb were collected via centrifugation at 20,000 × *g* for 90 min to remove unbound mAbs. Tri-NanoAb was then immersed in an imaging buffer and subjected to imaging using STORM (Abbelight) equipped with 3 Oxxius lasers at 488 nm, 532 nm and 647 nm (Oxxius) and NEO living imaging software (Abbelight). The hydrodynamic size and zeta potential of Tri-NanoAb were examined using a Zetasizer Nano ZS instrument (Malvern). The mass ratio of mFcγR1–MSA in FP-NA to mAbs was 10:1 and co-incubated for 16 h at 4 °C. The obtained multi-NanoAbs were used in subsequent cell and animal experiments.

### Association between cells and mAbs or Tri-NanoAb

αPDL1, αPD1 and αNKG2A were fluorescently labelled with Alexa Fluor 647/488/555 NHS ester (Thermo Fisher Scientific) using a previously described method. According to the manufacturer's protocol, B16F10 and $CD8^+$ T cells were stained with Calcein Violet 450 AM, and $1 \times 10^4$ labelled B16F10 cells or $1 \times 10^5$ labelled $CD8^+$ T cells were seeded in confocal dishes. Three fluorescent dye-labelled mAbs or Tri-NanoAb engineered from FP-NA with fluorescent dye-labelled mAbs (at a concentration of mAbs of 50 μg ml$^{-1}$) were added for 6 h at 37 °C. Finally, the cells were observed using a Zeiss LSM880 laser scanning confocal microscope with the ZEISS ZEN (black edition) system version 2.3.

### Tri-NanoAb facilitates the interaction between $CD8^+$ T cells and tumour cells

B16F10 cells and the isolated $CD8^+$ T cells were stimulated as described above. B16F10 cells were seeded into glass-bottom cell culture dishes (NEST) at a density of $5.0 \times 10^3$ cells per dish, and different numbers of DID-labelled $CD8^+$ T cells were added 12 h later, with mAbs Comb. or Tri-NanoAb (the combination of αPDL1, αPD1 and αNKG2A). After an

additional 4 h of incubation, the cells were washed with PBS to remove suspended T cells, and conjugation between T cells and tumour cells was visualized using a Zeiss LSM880 laser scanning confocal microscope with the ZEISS ZEN (black edition) system 2.3.

### The cytotoxicity of T cells in vitro

In this assay, $5.0 \times 10^3$ B16F10-Luc cells and $5.0 \times 10^4$ stimulated $CD8^+$ T cells were seeded in a 96-well TC-treated microtest assay microplate with a white flat bottom (Falcon). Subsequently, a combination of αPDL1, αPD1 and αNKG2A (mAbs Comb.) or PDL/PD1/NKG2A Tri-NanoAb were added. The final concentration of the mAbs ranged from 1 μg $ml^{-1}$ to 100 μg $ml^{-1}$, and the ratio of the 3 mAbs used was maintained at 1:1:1. Cell viability was assessed using a firefly luciferase assay kit (Thermo Fisher Scientific) according to the manufacturer's instructions.

### Therapy studies in tumour models

For the orthotopic breast cancer model, $5.0 \times 10^5$ 4T1 cells suspended in 75 μl of PBS were injected into the left second mammary fat pad of female BALB/c mice aged 7 weeks. When tumour volumes reached approximately 75–100 $mm^3$, the mice were randomly allocated to control and treatment groups. Intravenous administration of PBS, FP-NA/Iso (FP-NA immobilized IgG2a isotype control antibody), and a combination of αPDL1, αPD1 and αNKG2A (mAbs Comb.) or Tri-NanoAb (with a total mAb amount of 5 mg $kg^{-1}$, distributed in a 1:1:1 ratio) was conducted according to a schedule involving an injection every 3 days for a total of 3 injections (q3dx3). Tumours were measured bidaily using calipers, and their volumes were calculated using the following formula: $V = 0.5 \times \text{length}\,(L) \times \text{width}\,(W) \times \text{width}\,(W)$. Upon completion of the treatment, the mice were killed, and tumour images and weights were recorded.

For the subcutaneous melanoma model, $1.5 \times 10^5$ B16F10 or B16F10-Luc cells suspended in 75 μl of PBS were subcutaneously injected into the right flank of male C57BL/6 mice aged 7 weeks. When tumour volumes reached approximately 75–100 $mm^3$, the mice underwent treatment according to the consistent schedule mentioned above. Bioluminescence signals were recorded on days 7, 14 and 21 post-implantation using an in vivo imaging system (PerkinElmer IVIS Lumina III). The signals were analysed using the Living Image Software (PerkinElmer, V4.5.5). After completion of the treatment regimen, the mice were killed, and images and weights of the tumours were recorded. To investigate the impact of $CD8^+$ T cell and NK cell depletion on Tri-NanoAb's antitumour response, anti-CD8a antibody or anti-NK1.1 antibody (10 mg $kg^{-1}$) was intraperitoneally injected 1 day before tumour implantation, followed by additional injections on days 3, 7 and 11 post-implantation. Mice received Tri-NanoAb when the tumour size reached approximately 75 $mm^3$, and tumour growth and survival were recorded.

In another melanoma model, tumour-bearing mice were treated with PBS, a combination of αCD47 and αCSFR1, or Bi-NanoAb (with a total mAb amount of 5 mg $kg^{-1}$, administered in a 1:1 ratio), following a schedule of 3 injections every 3 days for a total of 3 injections (q3dx3). Tumour growth was monitored using calipers. The survival of tumour-bearing mice was monitored without any additional therapy following the completion of the three treatments.

For the MMTV-PyMT spontaneous breast tumour model, mice with tumours were euthanized, and their tumour tissues were finely dissected in PBS using surgical scissors. The fragments were then centrifuged at 150 × *g* for 3 min before being resuspended in 5 ml of tumour digestion solution and digested at 37 °C for 1 h. After filtering through a 40 μm cell strainer to obtain a single-cell suspension, red blood cells were removed using RBC lysis solution, and the remaining tumour cells were counted and adjusted to a concentration of $1 \times 10^7$ cells per ml. Finally, anaesthetized FVB/NCrl female mice (7 weeks old) were injected with 100 μl cell suspensions into their left second mammary fat pad (*36*). When tumour volumes reached approximately 75–100 $mm^3$, the mice were randomly assigned to control and treatment groups. PBS, a combination of αPDL1, αPD1 and αNKG2A (mAbs Comb.), or Tri-NanoAb (with a total mAb amount of 5 mg $kg^{-1}$, distributed in a 1:1:1 ratio) were intravenously administered to the mice according to a schedule involving an injection every 3 days for a total of 3 injections (q3dx3). Tumours were measured, and their volumes were calculated using the following formula: $V = 0.5 \times \text{length}\,(L) \times \text{width}\,(W) \times \text{width}\,(W)$.

A20-Luc cells ($1.0 \times 10^6$) suspended in 75 μl of PBS were intravenously injected into BABL/c mice for the leukaemia model. Mice were allocated into 2 groups 7 days after tumour progression was confirmed using IVIS systems. For the subcutaneous lymphoma model, $2.0 \times 10^6$ A20 cells suspended in 75 μl of PBS were subcutaneously injected into the right flank of BABL/c mice. PBS and CD3/CD19 Bi-NanoAb (with a total mAb amount of 5 mg $kg^{-1}$, distributed in a 1:1 ratio) were intravenously administered according to a schedule involving an injection every 3 days for a total of 2 injections (q3dx2). Bioluminescence signals were recorded using an in vivo imaging system (PerkinElmer IVIS Lumina III). Tumours in the subcutaneous lymphoma model were measured, and their volumes were calculated using the following formula: $V = 0.5 \times \text{length}\,(L) \times \text{width}\,(W) \times \text{width}\,(W)$.

For the orthotopic pancreatic cancer model, $5.0 \times 10^5$ Pan02-Luc cells were suspended in a 50 μl solution consisting of 50% Matrigel (BD Biosciences) and 50% PBS. Anaesthetized C57BL/6 mice were placed on a heating pad covered with a sterile drape. The flank skin of the mice was sterilized using a tincture of iodine and 70% ethanol. The general area of the spleen is located in the upper-left quadrant of the abdomen. Forceps were used to pinch the skin above the spleen, make an approximately 1 cm incision and pinch the smooth muscle on the top of the spleen. The peritoneal cavity was accessed using scissors. The caudal end of the spleen was grabbed and pulled out to locate the pancreatic tail. Then, the 50 μl cell suspension was injected into the bottom of the pancreas. The incision was closed with a 6–0 suture. Mice were allocated to 3 groups 9 days after tumour formation was confirmed using IVIS. PBS and a combination of αPDL1, αPD1, αNKG2A and α4-1BB (mAbs Comb.) or Tetra-NanoAb (with a total mAb amount of 5 mg $kg^{-1}$, distributed in a 1:1:1:1 ratio) were intravenously administered according to a schedule involving an injection every 3 days for a total of 2 injections (q3dx3). Bioluminescence signals were recorded using an in vivo imaging system (PerkinElmer IVIS Lumina III).

For the human melanoma model, human peripheral blood mononuclear cells (hu-PBMCs, $5 \times 10^6$ cells) were intravenously injected into 7-week-old NOD/ShiLtJGpt-*Prkdc*$^{em26Cd52}$*Il2r*$^{gem26Cd22}$/Gpt (hu-NCG) mice. The engraftment of hu-PBMCs was validated by FACS analysis by collecting mouse blood for anti-human CD45 staining (clone 2D1, 1:25 dilution). Subsequently, $2.5 \times 10^6$ A375 cells suspended in 75 μl of PBS were subcutaneously injected on the right flank of NCG mice with hu-PBMC engraftment. When tumour volumes reached approximately 75–100 $mm^3$, the mice were randomly assigned to control and treatment groups ($n = 6$). PBS and a combination of αPDL1, αPD1 and αTIGIT (mAbs Comb.) or Tri-NanoAb (with a total mAb amount of 5 mg $kg^{-1}$, distributed in a 1:1:1 ratio) were intravenously administered to the mice according to a schedule involving an injection every 3 days for a total of 3 injections (q3dx3). Tumours were measured bidaily using calipers, and their volumes were calculated using the following formula: $V = 0.5 \times \text{length}\,(L) \times \text{width}\,(W) \times \text{width}\,(W)$.

### Statistical analysis

All experiments were repeated at least twice with consistent results between repetitions. Multiple comparisons were performed using one-way and two-way analyses of variance (ANOVA), followed by a Tukey post hoc test, whereas two-group comparisons were conducted using two-tailed Student's *t*-test. Survival curves were analysed using the log-rank (Mantel–Cox) test. All results are presented as mean ± s.d., and

differences for which $P < 0.05$ were considered significant. Significance levels were defined as follows: NS (not significant, $P > 0.05$), $^{*}P < 0.05$, $^{**}P < 0.01$, $^{***}P < 0.001$ and $^{****}P < 0.0001$. $P$ values were analysed using GraphPad Prism 8 software (GraphPad Software) and are indicated in the figures.

### Reporting summary

Further information on research design is available in the Nature Portfolio Reporting Summary linked to this article.

## Data availability

The RNA-seq data from this study have been deposited and released in the NCBI Sequence Read Archive (SRA) with accession codes PRJNA1030777 (ref. 54) and PRJNA1030781 (ref. 55). Sequences of clean data were mapped to the mouse reference genome (version GRCm39). The data supporting the findings of this study are available within the paper and its Supplementary Information files. All data generated in this study, including source data and the data used to create the figures, are available from the corresponding authors upon reasonable request. Source data are provided with this paper.

## References


1. Elgundi, Z., Reslan, M., Cruz, E., Sifniotis, V. & Kayser, V. The state-of-play and future of antibody therapeutics. *Adv. Drug Deliv. Rev.* **122**, 2–19 (2017).
2. Mullard, A. Trispecific antibodies take to the clinic. *Nat. Rev. Drug Discov.* **19**, 657–658 (2020).
3. Jin, S. et al. Emerging new therapeutic antibody derivatives for cancer treatment. *Signal Transduct. Target. Ther.* **7**, 39 (2022).
4. Sawant, M. S., Streu, C. N., Wu, L. & Tessier, P. M. Toward drug-like multi-specific antibodies by design. *Int. J. Mol. Sci.* **21**, 7496 (2020).
5. Li, H., Saw, P. E. & Song, E. Challenges and strategies for next-generation bispecific antibody-based antitumor therapeutics. *Cell. Mol. Immunol.* **17**, 451–461 (2020).
6. Tiller, K. E. & Tessier, P. M. Advances in antibody design. *Annu. Rev. Biomed. Eng.* **17**, 191–216 (2015).
7. Yanakieva, D. et al. Beyond bispecificity: controlled Fab arm exchange for the generation of antibodies with multiple specificities. *mAbs* **14**, 2018960 (2022).
8. Wu, S., Wu, F. & Chen, X. Antibody-incorporated nanomedicines for cancer therapy. *Adv. Mater.* **34**, e2109210 (2022).
9. Liu, L. et al. Boosting checkpoint immunotherapy with biomaterials. *ACS Nano* **17**, 3225–3258 (2023).
10. Yu, M., Yang, W., Yue, W. & Chen, Y. Targeted cancer immunotherapy: nanoformulation engineering and clinical translation. *Adv. Sci.* **9**, e2204335 (2022).
11. Jiang, C. et al. Immunomodulating nano-adaptors potentiate antibody-based cancer immunotherapy. *Nat. Commun.* **12**, 1359 (2021).
12. Ye, Q. et al. Orchestrating NK and T cells via tri-specific nano-antibodies for synergistic antitumor immunity. *Nat. Commun.* **15**, 6211 (2024).
13. Kik, K., Bukowska, B. & Sicińska, P. Polystyrene nanoparticles: sources, occurrence in the environment, distribution in tissues, accumulation and toxicity to various organisms. *Environ. Pollut.* **262**, 114297 (2020).
14. Sivaram, A. J., Wardiana, A., Howard, C. B., Mahler, S. M. & Thurecht, K. J. Recent advances in the generation of antibody-nanomaterial conjugates. *Adv. Healthc. Mater.* **7**, 1700607 (2018).
15. Lu, J. & Sun, P. Structural mechanism of high affinity FcγRI recognition of immunoglobulin G. *Immunol. Rev.* **268**, 192–200 (2015).
16. Gravina, A. et al. Protection of cell therapeutics from antibody-mediated killing by CD64 overexpression. *Nat. Biotechnol.* **41**, 717–727 (2023).
17. Snyder, K. M. et al. Expression of a recombinant high affinity IgG Fc receptor by engineered NK cells as a docking platform for therapeutic mAbs to target cancer cells. *Front. Immunol.* **9**, 2873 (2018).
18. Brandsma, A. M. et al. Mechanisms of inside-out signaling of the high-affinity IgG receptor FcγRI. *Sci. Signal.* **11**, eaaq0891 (2018).
19. McArthur, M. J. et al. Cellular uptake and intracellular trafficking of long chain fatty acids. *J. Lipid Res.* **40**, 1371–1383 (1999).
20. Shechter, Y. et al. Newly designed modifier prolongs the action of short-lived peptides and proteins by allowing their binding to serum albumin. *Bioconjugate Chem.* **23**, 1577–1586 (2012).
21. Fang, Y., Tong, G. C. & Means, G. E. Structural changes accompanying human serum albumin's binding of fatty acids are concerted. *Biochim. Biophys. Acta* **1764**, 285–291 (2006).
22. Garcia-Martinez, R. et al. Albumin: pathophysiologic basis of its role in the treatment of cirrhosis and its complications. *Hepatology* **58**, 1836–1846 (2013).
23. Yardley, D. A. nab-active ingredient mechanisms of action and delivery. *J. Control. Release* **170**, 365–372 (2013).
24. Shroff, R. T. et al. active ingredient, active ingredient, and nab-active ingredient for the treatment of advanced biliary tract cancers: a phase 2 clinical trial. *JAMA Oncol.* **5**, 824–830 (2019).
25. Hama, M. et al. Evidence for delivery of active ingr. via a denatured-albumin transport system. *ACS Appl. Mater. Interfaces* **13**, 19736–19744 (2021).
26. Montfoort, N. et al. NKG2A blockade potentiates CD8 T cell immunity induced by cancer vaccines. *Cell* **175**, 1744–1755.e15 (2018).
27. André, P. et al. Anti-NKG2A mAb is a checkpoint inhibitor that promotes antitumor immunity by unleashing both T and NK cells. *Cell* **175**, 1731–1743.e13 (2018).
28. Salomé, B. et al. NKG2A and HLA-E define an alternative immune checkpoint axis in bladder cancer. *Cancer Cell* **40**, 1027–1043.e9 (2022).
29. Yoshihara, K. et al. Inferring tumor purity and stromal and immune cell admixture from expression data. *Nat. Commun.* **4**, 2612 (2013).
30. Jing, Y. et al. Multi-omics prediction of immune-related adverse events during checkpoint immunotherapy. *Nat. Commun.* **11**, 4946 (2020).
31. Shahabi, V. et al. Gene expression profiling of whole blood in ipilimumab-treated patients for identification of potential biomarkers of immune-related gastrointestinal adverse events. *J. Transl. Med.* **11**, 75 (2013).
32. Guerriero, J. L. et al. Class IIa HDAC inhibition reduces breast tumors and metastases through antitumor macrophages. *Nature* **543**, 428–432 (2017).
33. Robinson, H. R. et al. A CD19/CD3 bispecific antibody for effective immunotherapy of chronic lymphocytic leukemia in the ibrutinib era. *Blood* **132**, 521–532 (2018).
34. Fu, A. et al. Tumor-resident intracellular microbiota promotes metastatic colonization in breast cancer. *Cell* **185**, 1356–1372.e26 (2022).
35. Alshetaiwi, H. et al. Defining the emergence of myeloid-derived suppressor cells in breast cancer using single-cell transcriptomics. *Sci. Immunol.* **5**, eaay6017 (2020).
36. Ishihara, J. et al. Targeted antibody and cytokine cancer immunotherapies through collagen affinity. *Sci. Transl. Med.* **11**, eaau3259 (2019).
37. Klein, A. P. Pancreatic cancer epidemiology: understanding the role of lifestyle and inherited risk factors. *Nat. Rev. Gastroenterol. Hepatol.* **18**, 493–502 (2021).
38. Vincent, A., Herman, J., Schulick, R., Hruban, R. H. & Goggins, M. Pancreatic cancer. *Lancet* **378**, 607–620 (2011).
39. Chuprin, J. et al. Humanized mouse models for immuno-oncology research. *Nat. Rev. Clin. Oncol.* **20**, 192–206 (2023).

40. Morad, G., Helmink, B. A., Sharma, P. & Wargo, J. A. Hallmarks of response, resistance, and toxicity to immune checkpoint blockade. *Cell* **184**, 5309–5337 (2021).
41. Carlino, M. S., Larkin, J. & Long, G. V. Immune checkpoint inhibitors in melanoma. *Lancet* **398**, 1002–1014 (2021).
42. Kirchhammer, N., Trefny, M. P., Maur, P. A., Läubli, H. & Zippelius, A. Combination cancer immunotherapies: emerging treatment strategies adapted to the tumor microenvironment. *Sci. Transl. Med.* **14**, eabo3605 (2022).
43. Aschner, C. B. et al. A multi-specific, multi-affinity antibody platform neutralizes sarbecoviruses and confers protection against SARS-CoV-2 in vivo. *Sci. Transl. Med.* **15**, eadf4549 (2023).
44. Labrijn, A. F., Janmaat, M. L., Reichert, J. M. & Parren, P. Bispecific antibodies: a mechanistic review of the pipeline. *Nat. Rev. Drug Discov.* **18**, 585–608 (2019).
45. Tapia-Galisteo, A., Compte, M., Álvarez-Vallina, L. & Sanz, L. When three is not a crowd: trispecific antibodies for enhanced cancer immunotherapy. *Theranostics* **13**, 1028–1041 (2023).
46. Kosmides, A. K., Sidhom, J. W., Fraser, A., Bessell, C. A. & Schneck, J. P. Dual targeting nanoparticle stimulates the immune system to inhibit tumor growth. *ACS Nano* **11**, 5417–5429 (2017).
47. Au, K. M., Park, S. I. & Wang, A. Z. Trispecific natural killer cell nanoengagers for targeted chemoimmunotherapy. *Sci. Adv.* **6**, eaba8564 (2020).
48. Caaveiro, J. M., Kiyoshi, M. & Tsumoto, K. Structural analysis of Fc/FcγR complexes: a blueprint for antibody design. *Immunol. Rev.* **268**, 201–221 (2015).
49. Bruhns, P. & Jönsson, F. Mouse and human FcR effector functions. *Immunol. Rev.* **268**, 25–51 (2015).
50. Fanali, G. et al. Human serum albumin: from bench to bedside. *Mol. Aspects Med.* **33**, 209–290 (2012).
51. Verrecchia, T. et al. Non-stealth (poly(lactic acid/albumin)) and stealth (poly(lactic acid-polyethylene glycol)) nanoparticles as injectable drug carriers. *J. Control. Release* **36**, 49–61 (1995).
52. Schneider, D. et al. Trispecific CD19-CD20-CD22-targeting duoCAR-T cells eliminate antigen-heterogeneous B cell tumors in preclinical models. *Sci. Transl. Med.* **13**, eabc6401 (2021).
53. Harrison, C. Focus shifts to antibody cocktails for COVID-19 cytokine storm. *Nat. Biotechnol.* **38**, 905–908 (2020).
54. Fan, Y.-N. Engineering multi-specific nano-antibodies based on a versatile nano-adaptor for cancer immunotherapy. PRJNA1030777. *NCBI SRA* https://www.ncbi.nlm.nih.gov/bioproject/?term=PRJNA1030777 (2023).
55. Fan, Y.-N. Engineering multi-specific nano-antibodies based on a versatile nano-adaptor for cancer immunotherapy. PRJNA1030781. *NCBI SRA* https://www.ncbi.nlm.nih.gov/bioproject/?term=PRJNA1030781 (2023).

## Acknowledgements

This work was supported by the National Natural Science Foundation of China (52130301, J.W.; 32430059, J.W.; 32071380, S.S.), the National Key R&D Program of China (2021YFB3800900, S.S.; 2022YFC3401400, J.W.), the Science and Technology Program of Guangzhou, China (202103030004, J.W.), the Guangdong Basic and Applied Basic Research Foundation (2022B1515020058, S.S.) and the GJYC Program of Guangzhou City (2024D03J0001, J.W.).

## Author contributions

Y.-N.F., S.S. and J.W. designed the project. Y.-N.F. and S.S. designed all the experiments. Y.-N.F. performed most of the experiments. Y.-X.Q., F.-C.L., D.-K.Z. and T.-Y.T. contributed to the animal experiments. L.Z. amplified, produced and purified the fusion proteins. S.-Y.Y., Q.-N.Y. and X.-Y.H. performed the optimization of FP-NA preparation conditions and scaled up for production. G.-R.Y. helped with RNA-seq analysis. Y.-N.F., S.S. and J.W. wrote the paper. X.-Z.Y. provided suggestions for modification.

## Competing interests

The authors declare no competing interests.

## Additional information

**Supplementary information** The online version contains supplementary material available at https://doi.org/10.1038/s41551-025-01425-5.

**Correspondence and requests for materials** should be addressed to Song Shen or Jun Wang.

**Peer review information** *Nature Biomedical Engineering* thanks Xuesi Chen, Luo Kui and the other, anonymous, reviewer(s) for their contribution to the peer review of this work. Peer reviewer reports are available.

nature portfolio

Corresponding author(s): Jun Wang

Last updated by author(s): Apr 18, 2025

# Reporting Summary

Nature Portfolio wishes to improve the reproducibility of the work that we publish. This form provides structure for consistency and transparency in reporting. For further information on Nature Portfolio policies, see our Editorial Policies and the Editorial Policy Checklist.

## Statistics

For all statistical analyses, confirm that the following items are present in the figure legend, table legend, main text, or Methods section.

| n/a | Confirmed | |
|---|---|---|
| ☐ | ☒ | The exact sample size (*n*) for each experimental group/condition, given as a discrete number and unit of measurement |
| ☐ | ☒ | A statement on whether measurements were taken from distinct samples or whether the same sample was measured repeatedly |
| ☐ | ☒ | The statistical test(s) used AND whether they are one- or two-sided<br>*Only common tests should be described solely by name; describe more complex techniques in the Methods section.* |
| ☒ | ☐ | A description of all covariates tested |
| ☐ | ☒ | A description of any assumptions or corrections, such as tests of normality and adjustment for multiple comparisons |
| ☐ | ☒ | A full description of the statistical parameters including central tendency (e.g. means) or other basic estimates (e.g. regression coefficient) AND variation (e.g. standard deviation) or associated estimates of uncertainty (e.g. confidence intervals) |
| ☐ | ☒ | For null hypothesis testing, the test statistic (e.g. *F*, *t*, *r*) with confidence intervals, effect sizes, degrees of freedom and *P* value noted<br>*Give P values as exact values whenever suitable.* |
| ☒ | ☐ | For Bayesian analysis, information on the choice of priors and Markov chain Monte Carlo settings |
| ☒ | ☐ | For hierarchical and complex designs, identification of the appropriate level for tests and full reporting of outcomes |
| ☒ | ☐ | Estimates of effect sizes (e.g. Cohen's *d*, Pearson's *r*), indicating how they were calculated |

*Our web collection on statistics for biologists contains articles on many of the points above.*

## Software and code

Policy information about availability of computer code

| | |
|---|---|
| Data collection | Flow cytometry: FACSDiva software v 8.0.3; Confocal microscopy: ZEISS ZEN (black edition) system 2.3; ELISA: TECAN iControl (Version 2.0); Bioluminescent and fluorescent imaging: Living Image v4.5.5; Titration curves: MicroCal PEAQ-ITC control software (Version 1.1); STORM: NEO Livingimaging; DLS: Malvern Zetasizer Software v7.12; NanoFCM: NanoFCM Profession V2.0. |
| Data analysis | All statistical analyses were performed on Graphpad Prism 8.0.2;<br>Flow cytometry data were analyzed on FlowJo software V10.0.7;<br>Bioluminescent and fluorescence images were analyzed on Living Image v4.5.5;<br>Confocal images were analyze on ZEN2 (blue edition) and Fiji software v1.53c;<br>NEO Analysis was used for analysis STORM images;<br>RNA-seq analysis was analyzed on R software V4.2.2;<br>PPI analysis was facilitated by STRING V12.0 and Cytoscape software V3.10.1;<br>DPD simulation was performed by Materials Studio software Version 2020. |

For manuscripts utilizing custom algorithms or software that are central to the research but not yet described in published literature, software must be made available to editors and reviewers. We strongly encourage code deposition in a community repository (e.g. GitHub). See the Nature Portfolio guidelines for submitting code & software for further information.

## Data

Policy information about availability of data

All manuscripts must include a data availability statement. This statement should provide the following information, where applicable:

- Accession codes, unique identifiers, or web links for publicly available datasets
- A description of any restrictions on data availability
- For clinical datasets or third party data, please ensure that the statement adheres to our policy

The RNA-seq data in this study have been deposited and released at NCBI Sequence Read Archive (SRA) with accession code PRJNA1030777(https://www.ncbi.nlm.nih.gov/bioproject/?term=PRJNA1030777) and PRJNA1030781 (https://www.ncbi.nlm.nih.gov/bioproject/?term=PRJNA1030781). Sequences of clean data were mapped to the mouse reference genome (Version GRCm39). The data supporting the finding of this study are available within the paper and its Suplementary Information. All data generated in this study, including source data and the data used to generate the figures, are available from the corresponding authors upon reasonable reguest.

## Research involving human participants, their data, or biological material

Policy information about studies with human participants or human data. See also policy information about sex, gender (identity/presentation), and sexual orientation and race, ethnicity and racism.

| | |
|---|---|
| Reporting on sex and gender | N/A |
| Reporting on race, ethnicity, or other socially relevant groupings | N/A |
| Population characteristics | N/A |
| Recruitment | N/A |
| Ethics oversight | N/A |

Note that full information on the approval of the study protocol must also be provided in the manuscript.

# Field-specific reporting

Please select the one below that is the best fit for your research. If you are not sure, read the appropriate sections before making your selection.

☒ Life sciences ☐ Behavioural & social sciences ☐ Ecological, evolutionary & environmental sciences

For a reference copy of the document with all sections, see nature.com/documents/nr-reporting-summary-flat.pdf

# Life sciences study design

All studies must disclose on these points even when the disclosure is negative.

| | |
|---|---|
| Sample size | For in vitro studies, sample sizes were chosen on the basis of an initial pilot experiment and further based on similar experiments reported in previous publications (PMID: 30503208, PMID: 33649336). For in vivo experiments, the sample sizes were chosen to ensure they are sufficient to identify differences between groups with at least 80% power and a 5% significance level. Sample size was estimated on the basis of similar research reported in the literature (PMID: 30531990, PMID: 30503213). Details regarding sample size of all experiments are provided in the Methods section and figure legends. |
| Data exclusions | No data were excluded from the analyses. |
| Replication | All experiments were replicated at least twice individual replicates, unless stated otherwise, yielding similar results. |
| Randomization | For the in vivo animal study, mice were randomly allocated to each group in all experiments. For the other experiments, all samples were randomly assigned into experimental groups. |
| Blinding | The investigators were blinded during the tumor-size measurements, and other experiments were not blinded because all data were quantitatively measured with standard equipment. Blinding was not relevant to other experiments because the results are purely based on objective measurements. |

# Behavioural & social sciences study design

All studies must disclose on these points even when the disclosure is negative.

| | |
|---|---|
| Study description | N/A |
| Research sample | N/A |
| Sampling strategy | N/A |
| Data collection | N/A |
| Timing | N/A |
| Data exclusions | N/A |
| Non-participation | N/A |
| Randomization | N/A |

# Ecological, evolutionary & environmental sciences study design

All studies must disclose on these points even when the disclosure is negative.

| | |
|---|---|
| Study description | N/A |
| Research sample | N/A |
| Sampling strategy | N/A |
| Data collection | N/A |
| Timing and spatial scale | N/A |
| Data exclusions | N/A |
| Reproducibility | N/A |
| Randomization | N/A |
| Blinding | N/A |

Did the study involve field work? ☐ Yes ☒ No

# Reporting for specific materials, systems and methods

We require information from authors about some types of materials, experimental systems and methods used in many studies. Here, indicate whether each material, system or method listed is relevant to your study. If you are not sure if a list item applies to your research, read the appropriate section before selecting a response.

## Materials & experimental systems

| n/a | Involved in the study |
|---|---|
| ☐ | ☒ Antibodies |
| ☐ | ☒ Eukaryotic cell lines |
| ☒ | ☐ Palaeontology and archaeology |
| ☐ | ☒ Animals and other organisms |
| ☒ | ☐ Clinical data |
| ☒ | ☐ Dual use research of concern |
| ☒ | ☐ Plants |

## Methods

| n/a | Involved in the study |
|---|---|
| ☒ | ☐ ChIP-seq |
| ☐ | ☒ Flow cytometry |
| ☒ | ☐ MRI-based neuroimaging |

## Antibodies

Antibodies used

The following antibodies were used for FP-NA preparation and treatment. They are listed as antigen first, following by supplier, catalog number and clone/lot number as applicable.

1. Anti-mouse PD1, Bio X cell, cat. no. BP0146, Clone: RMP1-14;
2. Anti-mouse NKG2A/C/E, Bio X cell, cat. no. BE0321, Clone: 20D5;
3. Anti-mouse CSF1R, Bio X cell, cat. no. BE0213, clone: AFS98;
4. Anti-mouse CD47, Bio X cell, cat. no. BE0270, Clone: MIAP301;
5. Anti-mouse CD3, Bio X cell, cat. no. BE0261, Clone: KT30;
6. Anti-mouse CD8α, Bio X cell, cat. no. BE0004-1, Clone: 53-6.7;
7. Anti-mouse 4-1BB, Bio X cell, cat. no. BE0239, Clone: 3H3;
8. Anti-mouse 4-1BBL, Bio X cell, cat. no. BE0110, Clone: TKS-1;
9. Anti-mouse TIM-3, Bio X cell, cat. no. BE0115, Clone: RMT3-23;
10. Anti-mouse NK1.1, Bio X cell, cat. no. BE0036, Clone: PK136;
11. IgG2a isotype control, Bio X cell, cat. no. BE0089, Clone: 2A3;
12. Anti-mouse PDL1, BioLegend, cat. no. 153603, Clone: MIH6;
13. Anti-CD3ε antibody, BioLegend, cat. no. 100340, Clone: 145-2C11;
14. Anti-CD28 antibody, BioLegend, cat. no. 102116, Clone: 37.51.

The following primary or secondary antibodies were used for Western Blot/ELISA. They are listed as antigen first, following by supplier, catalog number and clone/lot number as applicable.

1. Anti-mouse FcγR1 antibody, Thermo Fisher Scientific, cat. no. MA5-29706, Clone: 27, 1:5,000 dilution;
2. Anti-mouse/human albumin antibody, Abcam, cat. no. ab207327, Clone: EPR20195, 1:5,000 dilution;
3. Anti-6 X His tag® antibody, Abcam, cat. no. ab18184, Clone: HIS.H8, 1:5,000 dilution;
4. Anti-human FcγR1 antibody, Abcam, cat. no. ab109449, Clone: EPR4623, 1:5,000 dilution;
5. Goat anti-rabbit IgG H&L (HRP), Abcam, cat. no. ab6721, polyclone, 1:10,000 dilution;
6. Goat anti-mouse IgG H&L (HRP), Abcam, cat. no. ab205719, polyclone, 1:10,000 dilution;
7. HRP-conjugated anti-albumin antibody, Sino Biological, cat. no. 68001-R101-H, Clone: #101, 1:1,000 dilution.

The following primary antibodies were used for flow cytometry/immunofluorescent staining. They are listed as antigen first, following by supplier, catalog number and clone/lot number as applicable.

1. Anti-CD16/32 antibody, BioLegend, cat. no. 101320, Clone 93, 1:50 dilution;
2. Brilliant Violet 510 anti-mouse CD45 antibody, BioLegend, cat. no. 110741, Clone: A20, 1:100 dilution;
3. Brilliant Violet 421 anti-mouse CD3 antibody, BioLegend, cat. no. 155617, Clone: KT3.1.1, 1:100 dilution;
4. Alexa Fluor® 700 anti-mouse NK-1.1 antibody, BioLegend, cat. no. 108730, Clone: PK136, 1:100 dilution;
5. Brilliant Violet 785 anti-mouse CD8 antibody, BioLegend, cat. no. 105043, Clone: GL-1, 1:100 dilution;
6. PE/Cyanine7 anti-mouse CD69 antibody, BioLegend, cat. no. 104512, Clone: H1.2F3, 1:100 dilution;
7. APC anti-mouse CD4 antibody, BioLegend, cat. no. 100516, Clone: RM4-5, 1:100 dilution;
8. PerCP/Cyanine5.5 anti-mouse CD25 antibody, BioLegend, cat. no. 101912, Clone: 3C7, 1:50 dilution;
9. PE anti-mouse FOXP3 antibody, BioLegend, cat. no. 126404, Clone: MF-14, 1:50 dilution;
10. Alexa Fluor 647 anti-mouse CD8a antibody, BioLegend, cat. no. 100724, Clone: 53-6.7, 1:100 dilution;
11. Alexa Fluor 647 anti-human CD3 antibody, BioLegend, cat. no. 300416, Clone: UCHT1, 1:50 dilution;
12. PerCP/Cyanine5.5 anti-human CD45 antibody, BioLegend, cat. no. 368503, Clone: 2D1, 1:25 dilution.

Validation

All antibodies are commercially available. Each antibody was validated for species and application, as appropriate, according to the manufacturer's website, and as supported by relevant citations on their product pages.

## Eukaryotic cell lines

Policy information about cell lines and Sex and Gender in Research

Cell line source(s)

The cell lines, including B16F10 murine melanoma cells, 4T1 murine breast cancer cells, Pan02 murine pancreatic cancer cells, A20 murine B-cell lymphoma cells, and A375 human melanoma cells were obtained from the American Type Culture Collection (ATCC). HEK293F was obtained from FuHeng BioLogy Co., LTD. CHOK10 was obtained from QuaCell Biotechnology, Co., Ltd. The construct expressing firefly luciferase (Luc) was introduced into B16F10, Pan02, and A20 cells by transfecting luciferase encoding lentiviral vectors. All tumor cells were cultured in Dulbecco's modified Eagle's medium (DMEM) (Gibco) or RPMI Medium 1640 (Gibco) supplemented with 10% fetal bovine serum (ExCell Bio) and 1% penicillin/streptomycin (Gibco). All cells were kept in a 37 degrees C ? incubator supplied with 5% of carbon dioxide.

Authentication

All cell lines were certified by the manufacturers. B16F10/Pan02/A20-Luc cells were checked by Firefly luciferase reporter gene detection kit.

Mycoplasma contamination

All cell lines were tested for mycoplasma contamination. No mycoplasma contamination was found.

Commonly misidentified lines
(See ICLAC register)

No commonly misidentified cell lines were used.

## Palaeontology and Archaeology

Specimen provenance

*Provide provenance information for specimens and describe permits that were obtained for the work (including the name of the*

| | |
|---|---|
| Specimen provenance | *issuing authority, the date of issue, and any identifying information). Permits should encompass collection and, where applicable, export.* |
| Specimen deposition | *Indicate where the specimens have been deposited to permit free access by other researchers.* |
| Dating methods | *If new dates are provided, describe how they were obtained (e.g. collection, storage, sample pretreatment and measurement), where they were obtained (i.e. lab name), the calibration program and the protocol for quality assurance OR state that no new dates are provided.* |

☐ Tick this box to confirm that the raw and calibrated dates are available in the paper or in Supplementary Information.

| | |
|---|---|
| Ethics oversight | *Identify the organization(s) that approved or provided guidance on the study protocol, OR state that no ethical approval or guidance was required and explain why not.* |

Note that full information on the approval of the study protocol must also be provided in the manuscript.

## Animals and other research organisms

Policy information about studies involving animals; ARRIVE guidelines recommended for reporting animal research, and Sex and Gender in Research

| | |
|---|---|
| Laboratory animals | Male C57BL/6 mice and female BALB/c and C57BL/6 (6-8 weeks old) were purchased from Hunan Silaikejingda Laboratory Animal Technology Co., Ltd. Friend virus B-type (FVB) mice were purchased from Beijing Vital River Lab Animal Technology Co., Ltd. NOD/ShiLtJGpt-Prkdcem26Cd52Il2rgem26Cd22/Gpt (NCG, Strain NO. T001475) were purchased from GemPharmatech Co., Ltd. MMTV-PyVT (FVB/N-Tg (MMTV-PyVT)634Mul/J) transgenic mice were generously gifted by Prof. Z. X. Lian from Guangdong Provincial People's Hospital. All mice were housed in pathogen-free conditions and kept in a room with controlled temperature (~22 degrees C) and humidity (50±15%) under 12 h light/dark cycle. |
| Wild animals | The study did not involve wild animals. |
| Reporting on sex | Only female mice were used in murine mammary carcinoma orthotopic model. |
| Field-collected samples | The study did not involve samples collected from the field. |
| Ethics oversight | All the animal experiments were approved by the Animal Care and Use Committee at South China University of Technology, and every effort was made to minimize suffering from experiments. |

Note that full information on the approval of the study protocol must also be provided in the manuscript.

## Clinical data

Policy information about clinical studies

All manuscripts should comply with the ICMJE guidelines for publication of clinical research and a completed CONSORT checklist must be included with all submissions.

| | |
|---|---|
| Clinical trial registration | *Provide the trial registration number from ClinicalTrials.gov or an equivalent agency.* |
| Study protocol | *Note where the full trial protocol can be accessed OR if not available, explain why.* |
| Data collection | *Describe the settings and locales of data collection, noting the time periods of recruitment and data collection.* |
| Outcomes | *Describe how you pre-defined primary and secondary outcome measures and how you assessed these measures.* |

## Dual use research of concern

Policy information about dual use research of concern

### Hazards

Could the accidental, deliberate or reckless misuse of agents or technologies generated in the work, or the application of information presented in the manuscript, pose a threat to:

| No | Yes | |
|---|---|---|
| ☒ | ☐ | Public health |
| ☒ | ☐ | National security |
| ☒ | ☐ | Crops and/or livestock |
| ☒ | ☐ | Ecosystems |
| ☒ | ☐ | Any other significant area |

## Experiments of concern

Does the work involve any of these experiments of concern:

| No | Yes | |
|---|---|---|
| ☒ | ☐ | Demonstrate how to render a vaccine ineffective |
| ☒ | ☐ | Confer resistance to therapeutically useful antibiotics or antiviral agents |
| ☒ | ☐ | Enhance the virulence of a pathogen or render a nonpathogen virulent |
| ☒ | ☐ | Increase transmissibility of a pathogen |
| ☒ | ☐ | Alter the host range of a pathogen |
| ☒ | ☐ | Enable evasion of diagnostic/detection modalities |
| ☒ | ☐ | Enable the weaponization of a biological agent or toxin |
| ☒ | ☐ | Any other potentially harmful combination of experiments and agents |

# Plants

Seed stocks

*Report on the source of all seed stocks or other plant material used. If applicable, state the seed stock centre and catalogue number. If plant specimens were collected from the field, describe the collection location, date and sampling procedures.*

Novel plant genotypes

*Describe the methods by which all novel plant genotypes were produced. This includes those generated by transgenic approaches, gene editing, chemical/radiation-based mutagenesis and hybridization. For transgenic lines, describe the transformation method, the number of independent lines analyzed and the generation upon which experiments were performed. For gene-edited lines, describe the editor used, the endogenous sequence targeted for editing, the targeting guide RNA sequence (if applicable) and how the editor was applied.*

Authentication

*Describe any authentication procedures for each seed stock used or novel genotype generated. Describe any experiments used to assess the effect of a mutation and, where applicable, how potential secondary effects (e.g. second site T-DNA insertions, mosiacism, off-target gene editing) were examined.*

# ChIP-seq

## Data deposition

☐ Confirm that both raw and final processed data have been deposited in a public database such as GEO.

☐ Confirm that you have deposited or provided access to graph files (e.g. BED files) for the called peaks.

Data access links
*May remain private before publication.*

*For "Initial submission" or "Revised version" documents, provide reviewer access links. For your "Final submission" document, provide a link to the deposited data.*

Files in database submission

*Provide a list of all files available in the database submission.*

Genome browser session
(e.g. UCSC)

*Provide a link to an anonymized genome browser session for "Initial submission" and "Revised version" documents only, to enable peer review. Write "no longer applicable" for "Final submission" documents.*

## Methodology

Replicates

*Describe the experimental replicates, specifying number, type and replicate agreement.*

Sequencing depth

*Describe the sequencing depth for each experiment, providing the total number of reads, uniquely mapped reads, length of reads and whether they were paired- or single-end.*

Antibodies

*Describe the antibodies used for the ChIP-seq experiments; as applicable, provide supplier name, catalog number, clone name, and lot number.*

Peak calling parameters

*Specify the command line program and parameters used for read mapping and peak calling, including the ChIP, control and index files used.*

Data quality

*Describe the methods used to ensure data quality in full detail, including how many peaks are at FDR 5% and above 5-fold enrichment.*

Software

*Describe the software used to collect and analyze the ChIP-seq data. For custom code that has been deposited into a community repository, provide accession details.*

# Flow Cytometry

## Plots

Confirm that:

☒ The axis labels state the marker and fluorochrome used (e.g. CD4-FITC).

☒ The axis scales are clearly visible. Include numbers along axes only for bottom left plot of group (a 'group' is an analysis of identical markers).

☒ All plots are contour plots with outliers or pseudocolor plots.

☒ A numerical value for number of cells or percentage (with statistics) is provided.

## Methodology

| | |
|---|---|
| Sample preparation | Tumor tissues were harvested, minced and incubated with RPMI-1640 medium containing 10% FBS (v/v), collagenase type I (1 mg/mL), hyaluronidase (100 μg/mL) and DNase I (100 μg/mL) at 37 degree C or 30 min with persistent agitation. Digested cells were passed through a 40-μm nylon mesh and collected by centrifugation at 800 g for 10 min, followed by ACK lysing buffer. Blood samples were collected into 1.5 ml centrifuge tubes containing sodium heparin, lysed with red blood cell lysis buffer, washed with PBS, and centrifuged at 400 g for 5 min to collect the cells. Cells were labelled with anti-surface marker antibodies for 30 min in the dark, preceded by blocking with anti-CD16/32 antibody at 4 degree C for 15 min. For intracelular staining, cells were first stained with surface antigen antibodies, fixed, and permeabilized using a commercial kit (eBioscience Foxp3/Transcription Factor Staining Buffer Set, Invitrogen, Carlsbad, CA, UsA) according to the manufacturer's instructions. The cells were then stained with antibodies for intracellular antigens and thoroughly washed. |
| Instrument | BD LSRFortessa™ flow cytometer |
| Software | BD FacsDiva v8.0, FlowJo software V10.0.7 |
| Cell population abundance | N/A |
| Gating strategy | In general, cells were first gated by FSC/SSC gates. Single cells were gated using FSC-H and FSC-A, and live/dead gates. These cells were further gated by CD45 for leukocytes. Next, gating for surface and intracellular antigens was performed based on the specific cells and markers to be analysed. Flow-cytometry gating strategies are provided in the Supplementary figures. |

☒ Tick this box to confirm that a figure exemplifying the gating strategy is provided in the Supplementary Information.

# Magnetic resonance imaging

## Experimental design

| | |
|---|---|
| Design type | *Indicate task or resting state; event-related or block design.* |
| Design specifications | *Specify the number of blocks, trials or experimental units per session and/or subject, and specify the length of each trial or block (if trials are blocked) and interval between trials.* |
| Behavioral performance measures | *State number and/or type of variables recorded (e.g. correct button press, response time) and what statistics were used to establish that the subjects were performing the task as expected (e.g. mean, range, and/or standard deviation across subjects).* |

## Acquisition

| | |
|---|---|
| Imaging type(s) | *Specify: functional, structural, diffusion, perfusion.* |
| Field strength | *Specify in Tesla* |
| Sequence & imaging parameters | *Specify the pulse sequence type (gradient echo, spin echo, etc.), imaging type (EPI, spiral, etc.), field of view, matrix size, slice thickness, orientation and TE/TR/flip angle.* |
| Area of acquisition | *State whether a whole brain scan was used OR define the area of acquisition, describing how the region was determined.* |

Diffusion MRI ☐ Used ☐ Not used

## Preprocessing

| | |
|---|---|
| Preprocessing software | *Provide detail on software version and revision number and on specific parameters (model/functions, brain extraction, segmentation, smoothing kernel size, etc.).* |
| Normalization | *If data were normalized/standardized, describe the approach(es): specify linear or non-linear and define image types used for transformation OR indicate that data were not normalized and explain rationale for lack of normalization.* |

Normalization template

*Describe the template used for normalization/transformation, specifying subject space or group standardized space (e.g. original Talairach, MNI305, ICBM152) OR indicate that the data were not normalized.*

Noise and artifact removal

*Describe your procedure(s) for artifact and structured noise removal, specifying motion parameters, tissue signals and physiological signals (heart rate, respiration).*

Volume censoring

*Define your software and/or method and criteria for volume censoring, and state the extent of such censoring.*

## Statistical modeling & inference

Model type and settings

*Specify type (mass univariate, multivariate, RSA, predictive, etc.) and describe essential details of the model at the first and second levels (e.g. fixed, random or mixed effects; drift or auto-correlation).*

Effect(s) tested

*Define precise effect in terms of the task or stimulus conditions instead of psychological concepts and indicate whether ANOVA or factorial designs were used.*

Specify type of analysis: ☐ Whole brain ☐ ROI-based ☐ Both

Statistic type for inference

*Specify voxel-wise or cluster-wise and report all relevant parameters for cluster-wise methods.*

(See Eklund et al. 2016)

Correction

*Describe the type of correction and how it is obtained for multiple comparisons (e.g. FWE, FDR, permutation or Monte Carlo).*

## Models & analysis

| n/a | Involved in the study |
|---|---|
| ☐ | ☐ Functional and/or effective connectivity |
| ☐ | ☐ Graph analysis |
| ☐ | ☐ Multivariate modeling or predictive analysis |

Functional and/or effective connectivity

*Report the measures of dependence used and the model details (e.g. Pearson correlation, partial correlation, mutual information).*

Graph analysis

*Report the dependent variable and connectivity measure, specifying weighted graph or binarized graph, subject- or group-level, and the global and/or node summaries used (e.g. clustering coefficient, efficiency, etc.).*

Multivariate modeling and predictive analysis

*Specify independent variables, features extraction and dimension reduction, model, training and evaluation metrics.*